Chapter 11

Cell, Stack and System Modelling

Mohammad A. Khaleel and J. Robert Selman

List of terms

c_i	mass fraction of species *i*
c_p	specific heat
$c_{r,electrode}$	reactant concentration at electrode
$c_{r,bulk}$	reactant concentration at gas channel
$c_{p,electrode}$	product concentration at electrode
$c_{p,bulk}$	product concentration at gas channel
d	half-thickness of the plate
D_h	hydraulic diameter
D_{ij}, $D_{O2\text{-}N2}$, $D_{H2\text{-}H2O}$	binary diffusion coefficients
D_{im}	multicomponent diffusion coefficient of species *i* in a mixture
$D_{eff(a)}$	anode effective diffusion coefficients
$D_{eff(c)}$	cathode effective diffusion coefficients
dr_y/dt	rate of mole change of species y (y = H_2, O_2, H_2O, CO, CO_2, CH_4)
dr_f/dt	rate of change due to forward reaction
dr_b/dt	rate of change due to backward reaction
E	Young's modulus
E_{eq} or E^o	the equilibrium (open circuit) voltage
E_{H2}	activation energy
E_{total}	total energy (delivered per unit time)
E^k	turbulent kinetic energy
F	Faraday constant
g	acceleration due to gravity
ΔG^o	standard free-energy change of a reaction (eq.8a)
ΔG^0_{shift}	standard Gibbs free-energy change of the shift reaction
h	heat transfer coefficient

h_1 and h_2	thickness of layer 1 and 2, respectively
ΔH	enthalpy of formation
I, i	current density
i_0	the exchange current density
i_{H2}	limiting current density due to H_2 transport
i_{O2}	limiting current density due to O_2 transport
i_c	concentration limiting current
k_1	rate constant for shift reaction
k_{H2}	rate constant for H_2 oxidation
k_{CO}	rate constant for CO oxidation
K_{shift}	equilibrium constant for the shift reaction
l	the length of the flow path
l_a, l_c	thickness of anode and cathode, respectively
m_1, m_2, m_3, m_4	reaction order parameter
m	Weibull parameter
n	unit vector normal to the boundary
p_{H2}	H_2 partial pressure in the anode fuel channel
p_{H2O}	H_2O partial pressure in the anode fuel channel
p_{O2}, $p_{O2,c}$	oxygen partial pressure in the cathode air channel
$p_{O2,a}$	oxygen partial pressure in the anode fuel channel
P	flow pressure
P_{cell}	cell power density
P_{stack}	stack power density
P_{ex}	electric power
p	stands for 'product'
Q	nonviscous volumetric heat generation term
Q_{gen}	heat generation
Q_{ohm}	ohmic heat
$Q_{irr,}$	heat generation due to irreversible process
$Q_{rev,a}$	reversible heat generation at the anode
$Q_{rev,c}$	reversible heat generation at the cathode
$Q_{rev,total}$	total reversible heat generation
Q_{vis}	viscous heat generation term
R	gas constant
R_i	ohmic resistance
Re	Reynolds number
r	stands for 'reactant'
S_i	entropy of species i ($i = O_2, O^{2-}$, el)
T	temperature
T_s and T_f	solid and fluid temperatures
ΔT	change in temperature
t	time
$\mathbf{U}_i$	diffusion velocity of species i
U_f	fuel utilisation
V	voltage

V_c	cathode porosities
V_a	anode porosities
V^{thn}	'thermoneutral voltage'
$\mathbf{v}$	fluid velocity
W	Weibull function, the probability of failure
W^v	viscous work
z	number of electrons participating in the electrode reaction
Greek letters	
α	anodic transfer coefficient
β	thermal expansion coefficient
γ_i	resistivity
ε_{el}	fuel cell electrical efficiency
η	overpotential or polarisation
η_A	anode polarisation
η_a	activation polarisation
η_C	cathode polarisation
η_c	concentration polarisation
η_{Ca}, η_{Cc}, η_{Aa} and η_{Ac}	cathode activation, cathode concentration, anode activation, and anode concentration polarisations, respectively
λ	thermal conductivity
μ_e	effective viscosity
ν	Poisson's ratio
ρ_i	density of the species *i*
σ_e	electronic conductivity
σ_{eff}	effective ionic conductivity
σ_{ion}	ionic conductivity
σ, σ_1, σ_x, σ_y	thermal stress
σ_0	material-specific characteristic stress of the Weibull function
τ_a and τ_c	anode and cathode tortuosities
τ_i	non-Newtonian viscous losses
Φ	electrical potential
ω_i	rate of production of species *i*
Ω_k	kth direction momentum source term

11.1 Introduction

Mathematical models that predict performance can aid in understanding and development of solid oxide fuel cells (SOFCs). A mathematical simulation of a SOFC is helpful in examining issues such as temperatures, materials, geometries, dimensions, fuels, and fuel reformation and in determining their associated performance characteristics. When physical properties or reaction kinetics are not known reliably, they can be estimated by fitting performance data on small-size, laboratory-scale cells to a mathematical model. The performance of a

small-size, laboratory-scale cell, by fitting an appropriate model, can yield input parameters for the performance of a larger cell or stack. This cell or stack simulation can be used to determine the effects of various design and operating parameters on the power generated, fuel conversion efficiency, maximum cell temperature reached, stresses caused by temperature gradients, and the effects of thermal expansion for electrolytes, electrodes, and interconnects.

Thus, modelling is an important tool in design optimisation, helping to answer important practical questions such as what air and fuel flow rates must be used to avoid excessive temperature or pressure drop. On the other hand, by providing answers to questions such as how much the electrical properties of the cell materials must be improved, simulations at the cell and electrode level can guide the development of new and improved materials. Mathematical simulation, therefore, has the potential to guide technology development, test the significance of various design features, assess the effectiveness of developments in materials or fabrication procedures, and select optimum operating conditions from a set of feasible parameters.

Various modelling approaches exist. The modelling may focus on individual thermal-mechanical, flow, chemical, and electrochemical subsystems or on coupled integrated systems. Because the subsystems are typically characterised by different length scales, modelling may also take place on different levels, ranging from the atomistic/molecular-level via the cell component-level, the cell-level to the stack-level, and finally to the system-level performance simulations.

This chapter discusses SOFC modelling primarily from the viewpoint of cells and stacks, although some information on system modelling and more extensive information on electrode modelling are also presented. After an introductory discussion of modelling levels, the SOFC cell and stack are first examined from the viewpoint of fluid dynamics and transport phenomena (SOFC as a heat and mass exchanger). This is followed in Section 11.3 by an exposition of electrochemical modelling at the 'continuum level', suitable for integration into modelling of full-scale stacks (SOFC as an electrochemical generator). In Section 11.4, the chemical reactions depending on fuel composition and the heat effects associated with their electrochemical conversion are discussed in detail (SOFC as a chemical reactor). Section 11.5 discusses cell- and stack-level modelling; and Section 11.6 briefly describes major approaches in SOFC system modelling (SOFC as a system component); Section 11.7 links the thermal analysis of the SOFC cell and stack with the modelling of thermal stresses; and Section 11.8 discusses in more detail the electrochemical modelling at the μm level suitable for electrode design and microstructure. Finally, Section 11.9 sketches possible approaches of molecular modelling suitable for elucidating kinetic and mechanistic issues relevant to SOFC performance.

11.2 Flow and Thermal Models

In a fuel cell operation, the flow, thermal, chemical, and electrochemical systems are intrinsically coupled. Heat generation and absorption affect the temperature

distribution and gas flow rate. Undesirable or even dangerous operating conditions may arise from the flow distribution [1]. Due to differences in coefficients of thermal expansion, temperature gradients during transient or stationary operation cause stresses that may lead to failure. Interdiffusion of materials used for the anode, the electrolyte, and the cathode may lead to gradual performance degradation. In order to calculate flow and temperature, the conservation laws in fluid mechanics are used [2].

11.2.1 Mass Balance

A species' mass in a reacting mixture of gases is determined by solving the species continuity equations:

$$\partial\rho_i/\partial t + \nabla\cdot[\rho_i(\mathbf{v} + \mathbf{U}_i)] = \omega_i \tag{1}$$

where ρ_i is the species density, $\mathbf{v}$ is the fluid velocity, $\mathbf{U}_i$ is the species diffusion velocity, t is time, and ω_i is the rate of production of species i due to chemical (or electrochemical) reactions. The mass flux of species i ($\rho_i\ \mathbf{U}_i$) due to diffusion can be approximated for most applications using Fick's law:

$$\rho_i\mathbf{U}_i = -\rho D_{im}\nabla c_i \tag{2}$$

where c_i is the species mass fraction (ρ_i/ρ), and D_{im} is the multicomponent diffusion coefficient of species i in the mixture. D_{im} is a weighted average of binary diffusion coefficients D_{ij}, that is, of the diffusion coefficients of species i with respect to each of the other species, j. Depending on the composition of the gas mixture, D_{im} can often be assumed to remain fairly constant. If there is one dominant species, k, in the mixture, the multicomponent diffusion coefficient D_{im} may often be approximated by the binary diffusion coefficient D_{ik}.

11.2.2 Conservation of Momentum

Mass balances must be used with the flow pattern (known *a priori* from theory or experimental measurements) to establish species concentrations and fluxes at any point in the fuel cell. When the flow pattern is *a priori* unknown, conservation-of-momentum equations (also called equations of motion) must be used with mass balance equations to establish the velocity and concentration profiles. Conservation of momentum for gases leads to the following equations (Navier–Stokes equations), in which k represents one of the three orthogonal directions in the coordinate system (x, y, and z):

$$\partial(\rho v_k)/\partial t + \nabla\cdot(\rho v_k\mathbf{v}) = \rho g_k - \partial P/\partial x_k + \nabla\cdot(\mu_e\nabla v_k) + \Omega_k + \tau_k \tag{3}$$

Here P is the pressure, g is the acceleration due to gravity, and μ_e is the effective viscosity. The term τ_k represents other than Newtonian viscous losses and may be

neglected for SOFC flows. A user-defined source term, Ω_k, can be used to represent in- and outflows due to electrode reactions at the boundary of the flow field.

Equation (3) provides details of gas flow movements. The full treatment requires a rigorous computational fluid dynamics (CFD) tool. Startup and transient processes as well as variations in certain operating parameters may have a sizeable effect on flow and concentration profiles, but the effect on overall electrochemical performance of the cell is not necessarily of the same order. Sometimes it is desirable to make a simplification such as assuming laminar flow to reduce the computation cost and allow quick estimates of certain flow properties. For example, the pressure drop of a laminar flow through a channel can be estimated as

$$\Delta P = (1/2)\rho v^2 fl/(ReD_h) \tag{4}$$

where Re is the D_h-based Reynolds number, D_h is the hydraulic diameter, l is the length of the flow path, and f depends on the shape of the cross section of the channel, e.g., $f = 56.8$ and 64 for a square and a round channel, respectively [3]. Such simplification can reduce the computation cost significantly [4].

11.2.3 Energy Balance

The temperature field and local heat fluxes in the gas phase are governed by the energy balance:

$$\partial(\rho c_p T)/\partial t + \nabla\cdot(\rho c_p T\mathbf{v}) = \nabla\cdot(\lambda\nabla T) + Q + \partial P/\partial t + Q_{vis} + W^v + E^k \tag{5}$$

Here c_p is specific heat, λ is thermal conductivity, Q is the nonviscous volumetric heat generation term, Q_{vis} is the viscous heat-generation term, W^v is viscous work, and E^k is turbulent kinetic energy. The volumetric heat source Q represents heat generation by the electrochemical reactions (planar heat sources being expressed on volumetric basis), chemical reactions (e.g., hydrocarbon reforming and CO water shift reaction), and Joule heating (due to ohmic resistance of electrolyte and electrodes). Without the last four terms, Eq. (5) also applies to the solid components of the fuel cell. These components consist of the positive electrode, the electrolyte, and the negative electrode (PEN) elements and the interconnect (IC) or bipolar plate. The PEN is sometimes assigned lumped properties for heat transfer modelling.

Heat transfer between cell components must also be accounted for, either as boundary conditions of Eq. (5) (boundary heat flows) or as a volumetric heat source (contributing to Q in Eq. (5)). These heat source terms due to interfacial heat transfer occur mainly in two ways [5]:

- Between cell component layers and flowing gas streams, e.g., between the anode or anode side of the PEN and the fuel gas stream or between the interconnect and the oxidant gas stream. This type of heat transfer is best described in terms of convective heat transfer coefficient h.

- Between adjacent solid layers with different thermal conductivities, λ_i (where i = cathode, anode, electrolyte, or interconnect). This type of heat transfer may be folded into a lumped effective conductivity, for example, for the PEN.

Alternatively, the heat transfer from the fuel gas stream to the oxidant gas stream via a solid layer such as the PEN element or the interconnect may be described in terms of an overall heat transfer coefficient.

For convective heat transfer at the boundary between a solid layer and a fluid, the following continuity condition may be imposed [6]:

$$\lambda(x)\nabla T_s(x)\cdot\mathbf{n} = h[T_f(x) - T_s(x)] \tag{6}$$

where $\mathbf{n}$ is the unit vector normal to the boundary, h is the heat transfer coefficient, and $T_s(x)$ and $T_f(x)$ are the temperatures of the solid and fluid, respectively, at location x on the boundary. Heat transfer may also take place by radiation from solid to gas phase or from solid to solid across a gas phase. This can usually be represented by variants of Eq. (6). Radiative heat transfer is especially important in higher temperature (900–1000°C) SOFC systems, for example, the tubular design SOFC generator [7,8].

For steady-state simulation, the equations above are simplified by deleting the time-dependent terms. However, the general forms are necessary for simulating transient operating conditions such as startup and 'load' variation, i.e., change in electrical output.

The combined flow and thermal models can be a powerful tool for addressing various SOFC design issues. For example, during fast startup or fast cool-down, which may be needed in automotive applications, thermal stresses that develop within the fuel-cell stack must not exceed acceptable levels. It is therefore necessary to model in detail the gas flows as well as heat and mass transfer throughout the fuel-cell stack to analyse the transient temperature distribution. The latter, in turn, may be used to predict the thermal stresses.

As an example, Figure 11.1 shows a typical planar cell stack model geometry [9]. The upper-left portion of the figure shows the full stack geometry. Preheated air is introduced at the bottom left side of the stack. The air travels across the interconnect channels, is further heated in contact with the PEN, and exits downward at right. In the fuel electrode (anode) side manifolds, as in the air electrode manifold, the outlet manifold is wider than that at the inlet. The 'zoom' view of the stack at the upper right in Figure 11.1 shows more detail of the grid. Details of the individual flow channels are simulated using a porous media model in the active area.

Obtained using the commercial computational fluid dynamics (CFD) software, STAR-CD, Figure 11.2 shows the temperature distribution within the interconnect which is subject to the largest temperature gradient, 5 minutes after startup.

Predictions of the stress created by thermal gradients within the stack can be used to establish control parameters for transient operations and to minimise

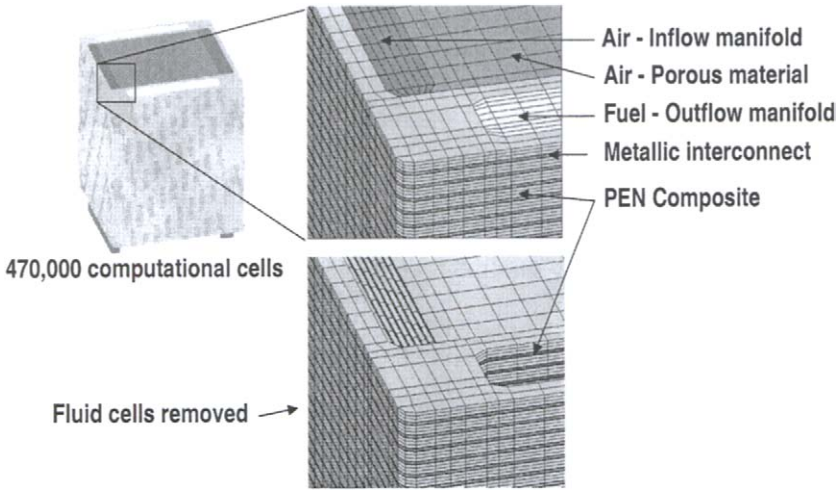

Figure 11.1. Stack model geometry for combined flow and thermal calculations.

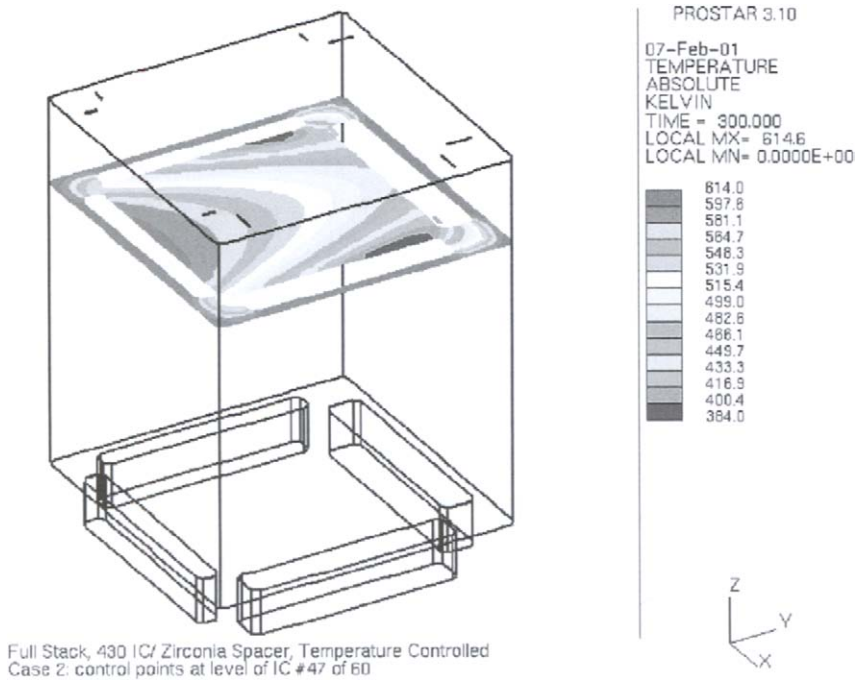

Figure 11.2 Temperature over interconnect 5 minutes after startup.

thermal stresses. Knowledge of thermal stress patterns can also provide guidance for geometry changes that may help to reduce stresses. The dimensioning of the individual PEN and IC elements is dictated in large part by the thermal stresses that develop during startup, caused by the thermal gradients within each

element and depending on the mismatch in coefficients of thermal expansion between cell components. The configuration of the manifolds and overall cell dimensions can be modified based on the thermal stress results. The simulation can also be used to optimise the stack geometry for flow uniformity.

11.3 Continuum-Level Electrochemistry Model

One of the most important aspects of SOFC design is the voltage and current distribution in the PEN. This couples with the temperature distribution from the flow model and also with the electrochemical reactions at the electrodes. The electrochemical process generates electrical power and heat, but excessive heat generation must be avoided since it may cause thermal stresses affecting the structural stability of the SOFC.

At the effective property or continuum level, the simulation of electrode and cell performance basically requires only a parameterised electrochemical model. Such an electrochemical model is usually described as a current–voltage relation, or I–V curve, for a single cell, in terms of parameters that are effective cell properties and operational parameters. The I–V relation describes the voltage (potential) loss at a specified current with respect to the ideal thermodynamic performance, which is called overpotential or polarisation (η). This cell I–V curve is specific for the materials, structural characteristics, and operational parameters (gas compositions, pressure, temperature) of a given PEN element.

As an analogy to mass and energy balances, one can write a potential balance of the fuel cell as follows [10]:

$$V(i) = E_{eq} - iR_i - \eta_C - \eta_A = E_{eq} - iR_i - \eta_{Ca} - \eta_{Cc} - \eta_{Aa} - \eta_{Ac} \tag{7}$$

Here E_{eq} is the equilibrium (open circuit) voltage, or emf (electromotive force) of the cell, i is the current density, iR_i is the ohmic potential drop, and η_C and η_A are the polarisation of the cathode and the anode, respectively. As shown in Eq. (7) each of the polarisation may be further split in an activation-related contribution (subscript a) and a concentration (i.e., diffusion) related contribution (subscript c).

The thermodynamic cell potential, E_{eq}, depends on reactant and product partial pressures as well as temperature. For example, for the hydrogen/oxygen fuel cell

$$E_{eq} = -\frac{\Delta G^0}{2F} + \frac{RT}{4F}\ln\frac{P_{O_2}P_{H_2}^2}{P_{H_2O}^2} = E^0 + \frac{RT}{4F}\ln\frac{P_{O_2}P_{H_2}^2}{P_{H_2O}^2} \tag{8a}$$

where R is the gas constant, T is the temperature, and F is the Faraday constant. ΔG° is the standard free-energy change of the reaction $H_2 + 1/2O_2 \rightarrow H_2O$; i.e., the free-energy change when reacting species and products are all at the standard pressure of 1 atm. The first term on the right-hand side of Eq. (8a),

denoted by $E°$, is therefore called the standard cell potential or standard emf. It depends only on temperature. In the second term on the right-hand side of Eq. (8a), p_{O2} is an abbreviation of $p_{O2,c}$ for notational simplicity. The quantities p_{H2} and p_{H2O} are, respectively, the H_2 and H_2O partial pressures in the anode fuel channel.

In the most general way, one can express the thermodynamic cell potential of an SOFC as the cell potential of an oxygen concentration cell using the Nernst equation:

$$E_{eq} = (RT/4F)\ln(p_{O2,c}/p_{O2,a}) \tag{8b}$$

In Eq (8b), $p_{O2,c}$ and $p_{O2,a}$ represent the oxygen partial pressures in the cathode air channel and anode fuel channel, respectively. Notice from Eq. (8b) that air leakage reduces the open-circuit voltage and is detrimental to cell operation. Good sealing technology is required to minimise the leakage.

In Eq. (7), R_i represents the total area specific ohmic resistance. R_i is the sum of the cathode, electrolyte, anode, interconnect, and contact ohmic resistances expressed in $\Omega\ m^2$. Typically, R_i is dominated by the electrolyte resistance and decreases with increasing operating temperature. To account for any electronic conductivity in the electrolyte, the effective ohmic resistance should be used in Eq. (7). The effective conductivity depends on the applied voltage and can be expressed as a correction to the ionic conductivity, σ_{ion}, by a term involving the electronic conductivity, σ_e as follows [11,12]:

$$\sigma_{eff} = \sigma_{ion} - \sigma_e/[\exp(2eV/kT) - 1]/[1-\exp(-2e(E_0 - V)/kT)]\} \tag{9}$$

The final terms in Eq. (7), η_{Ca}, η_{Cc}, η_{Aa} and η_{Ac}, are the cathode activation, cathode concentration, anode activation, and anode concentration polarisations, respectively. In general, their dependence on the current density is nonlinear, although at low polarisation they may be approximated by linear relationships.

The activation polarisation terms are controlled by the electrode reaction kinetics of the respective electrodes. They represent the voltage loss incurred due to the activation necessary for charge transfer. The activation polarisation, η_a, is usually related to the current density by the phenomenological Butler–Volmer equation [13]:

$$i = i_0\{\exp[-\alpha zF\eta_a/RT] - \exp[(1 - \alpha)zF\eta_a/RT]\} \tag{10a}$$

In this equation, i_0 is the exchange current density, α is the anodic transfer coefficient ($0 < \alpha < 1$), and z is the number of electrons participating in the electrode reaction. The exchange current density corresponds to the dynamic electron transfer rate at equilibrium, which is thermally activated. Therefore, the exchange current density can be expressed as $i_0 = P_x \exp(-E_{act}/RT)$, where the prefactor, P_x, and the activation energy, E_{act}, are properties specific for the electrode-electrolyte interface in question. The kinetic properties (i_0, α, z, P_x, E_{act})

depend not only on the materials forming the reaction interface but also on its microstructure[13,14].

The reasons for the importance of microstructure are twofold. Electrode reactions are interfacial reactions, i.e., surface bound, and therefore intrinsically slow compared with the reactions of gases. Moreover, in an SOFC they must take place at particular locations on the electrode–electrolyte interface, namely at or near a triple-phase boundary (TPB), where solid electrocatalyst, electrolyte, and gaseous reactants or products meet. In a typical SOFC porous electrode, the TPB is geometrically a serpentine line. The TPB by itself would form an extremely limited 'area' available for electron transfer. However, in SOFC electrodes the electron transfer step is only one of several steps in a reaction mechanism that may be quite complicated (as discussed in Chapter 9 and further referred to in Section 11.8). At the microscopic level, the active area of SOFC electrodes appears to be a nm-to-μm-wide zone bordering the TPB where surface diffusion of intermediate reactants or product species occurs. Nevertheless, the entire internal area of a porous electrode usually is not active. Typically, SOFC electrodes must have a reaction surface large enough to generate an internal current density (usually called transfer current density and denoted j) that is two to four orders of magnitude smaller than the projected (or external) current density at the electrode. Thus, to reduce the activation losses at an SOFC electrode, a large internal surface area is needed.

Therefore, in simplified continuum treatment of the electrochemical performance, e.g., in the potential balance (Eq. (7)), the activation polarisation is frequently calculated from Eq. (10a) by dividing the projected current density, i, by a dimensionless quantity, a, which represents the ratio of active internal area to external area:

$$j = \mathrm{i}/a = i_0\{\exp[-\alpha zF\eta_a/RT] - exp[(1-\alpha)zF\eta_a/RT]\} \qquad (10b)$$

The parameter a is specific for a given electrode microstructure and may be estimated from known or estimated microstructural parameters, physicochemical surface area measurements (e.g., by the BET technique, yielding total pore volume), or special-purpose electrochemical measurements (which yield the product $\mathrm{i}_0 a$). However, a is rarely known accurately and may vary significantly with current load. Electrode-level models may be used to determine this variation and calculate polarisation without recourse to Eq. (10b) (see Section 11.8).

In practice, the activation loss of the SOFC cathode is larger than that of the anode; that is, the cathode reaction has a smaller $i_0 a$ than the anode reaction. In fact, greater kinetic limitation of oxygen reduction than of hydrogen oxidation is common to all types of fuel cells at high (e.g. 1000°C) as well as low (ambient) temperatures.

The concentration polarisation is the voltage loss associated with the resistance to transport of reactant species to and product species from the reaction sites. This transport occurs by diffusion because convection is negligible in the pores of SOFC electrodes. The concentration difference between the bulk gas and the gas contacting the reaction site forms a concentration cell

whose cell voltage (emf), opposing the overall SOFC voltage, is observed as a voltage loss contribution, i.e., concentration polarisation. Thus, oxygen partial pressure in the cathode pores near the cathode/electrolyte is lower than that in the air channel. The more difficult the transport of oxygen through the porous medium, the greater the concentration polarisation at the cathode. Thus, a thick cathode in cathode-supported cells gives rise to high concentration polarisation even at moderate current densities. To lower concentration polarisation at high current densities to acceptable levels, the cathode should be as thin as practically feasible and the porosity and pore size as large as possible.

Excessive mass transfer resistance may cause a current limitation if the reactant concentration at the reaction site becomes small. In the extreme, that concentration may become zero (or rather, negligibly small). The current, in that case, reaches a plateau called the limiting current for the reactant species in question. With a number of simplifying assumptions, the limiting current concept can be used to derive a simple one-parameter expression for the concentration polarisation:

$$\eta_c = (RT/nF))\ln(1 - i/i_c) \tag{11}$$

Here i_c is the limiting current for the reacting species, i.e., O_2 for the cathode, with n = 4, and H_2 or CO for the anode, with n = 2 [9]. The limiting current of a species depends on its diffusivity in the surrounding gas mixture, its partial pressure, and the porosity, tortuosity, and thickness of the electrode. For H_2 fuel, the limiting current density can be calculated [15] as:

$$i_{H2} = 2p_{H2}D_{eff(a)}/(Cl_a) \tag{12}$$

while for air as oxidant, the O_2 limiting current density is

$$i_{O2} = (p_{O2}D_{eff(c)}/Cl_c)[P/(P - p^0_{O2})] \tag{13}$$

where P is the air pressure and l_a and l_c are respectively the anode and cathode thickness. The effective diffusion coefficients are given in terms of binary diffusion coefficients, porosities ($V_{c/a}$), and tortuosities ($\tau_{c/a}$):

$$D_{eff(c)} = V_c D_{O2-N2}/\tau_c \tag{14a}$$

$$D_{eff(a)} = V_a D_{H2-H2O}/\tau_a \tag{14b}$$

Analogous results can be obtained with CO as fuel. Because the anode binary diffusion coefficient, $D_{H2\text{-}H2O}$, is about four times that of the cathode counterpart, $D_{O2\text{-}N2}$, the cathode would have a much larger concentration polarisation than that of the anode for similar thickness, porosity, and tortuosity. Fairly thick anodes may be used without incurring excessive voltage loss. This is one of the reasons why anode-supported designs are preferred over cathode-supported designs in the thin-electrolyte intermediate temperature SOFCs.

As discussed above, the I–V relation of a PEN element depends on material properties and electrode structures as well as on operating parameters such as gas composition, pressure, and temperature. Using a simple first-order electrochemical model and the potential balance, Eq. (7), combined with simplified expressions for the various polarisation contributions such as Eqs. (8a), (10b), and (11)–(14b), I–V curves can be predicted. These predicted curves may be used to fit experimental I–V data and deduce, from an optimal fit, certain material and structure properties such as R_i and i_0a, which cannot be measured directly. In cells with sizable electrode area, which tend to have appreciable fuel and oxidant utilisation, temperature and gas partial pressures are local quantities dependent on the extent of the electrochemical and chemical conversion (i.e., the fuel and oxidant utilisations). The electrochemical model predicting the I–V curve simultaneously yields the current distribution, temperature distribution, and other quantities of interest.

Figure 11.3 shows the theoretical and experimental I–V relations of a small-size cell (considered isothermal) for different fuel compositions at a set of temperatures [14]. The material properties were obtained by fitting the theory to the experimental data for 97% H_2 + 3% H_2O fuel. As shown, the simplified theory can predict variation in the I–V curve with fuel composition reasonably well.

To obtain accurate information about microstructural characteristics of SOFC electrodes, a set of experimental i–η curves for a given electrode may be fitted, similar to Figure 11.3, against predictions of a more complex porous electrode model, as discussed in Section 11.8.

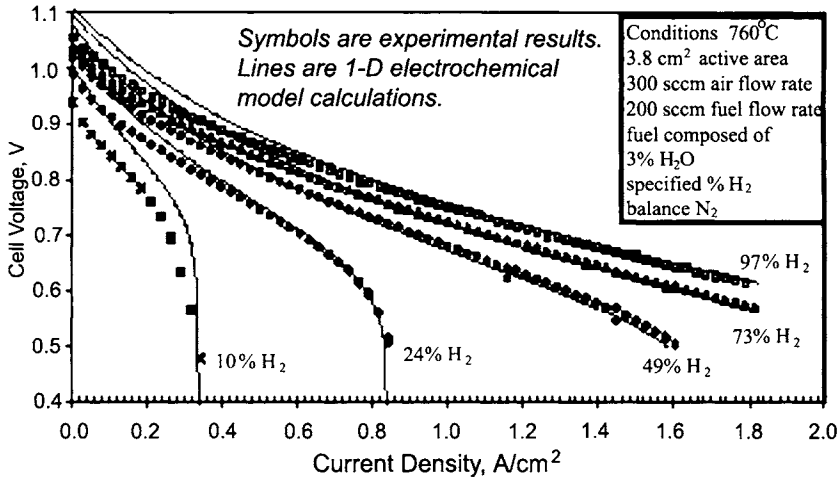

Figure 11.3. Predicted and measured cell I–V curves [14].

11.4 Chemical Reactions and Rate Equations

When fuel cells are operating, the heat generation rate (the source term needed in the thermal-fluid model) depends on the rates of the various chemical and

electrochemical reactions. These reactions are not always simple; methane fuel, for example, in the presence of steam may undergo steam reforming upstream of the electrode reaction sites, so the overall heat generation may be due to a multitude of anode reactions such as

$$H_2 + O^{2-} \rightarrow H_2O + 2e^- \tag{15a}$$

$$CO + O^{2-} \rightarrow CO_2 + 2e^- \tag{15b}$$

$$CH_4 + H_2O \rightarrow 3H_2 + CO \tag{15c}$$

$$CO + H_2O \rightarrow CO_2 + H_2 \tag{15d}$$

The cathode reaction, on the other hand, has a single stoichiometry:

$$1/2O_2 + 2e^- \rightarrow O^{2-} \tag{15e}$$

The heat source is related to the enthalpy change of the reactions, and the free-energy change of reactions (15a) and (15b) combined with (15e) determines the fuel cell Nernst potential. If chemical equilibrium is achieved in the system, the fuel composition, heat generation, and Nernst potential can be determined from thermodynamic theory. However, chemical equilibrium is usually not attained. In such cases, fuel composition and other information cannot be rigorously determined and must be approximated. The details of the reaction mechanism are complicated and usually not well understood, both for electrochemical and chemical reactions.

For example, anodic hydrogen oxidation probably involves dissociative hydrogen adsorption on the electrocatalyst (e.g., nickel) surface, surface diffusion of hydrogen adatoms, electron transfer under oxidation of H adatoms by an oxide ion at an adjacent active reaction site, and desorption of the H_2O molecule formed. Unstable and bulk unknown species such as OH may function as reaction intermediates. In chemical reactions, too, intermediates may play a role. Partial oxidation pathways for CH_4 may exist: e.g., $CH_4+O \rightarrow CH_2O+H_2$ and $CH_4+O \rightarrow CH_3OH$, resulting in the formation of chemicals such as CH_3OH or CH_2O with concomitant energy loss for the SOFC. Similarly, reaction intermediates such as O adatoms or adions may play a role.

Therefore, when equilibrium cannot be plausibly assumed, apparent kinetic parameters (effective rate constants) must be used to express the reaction rate. The parameters that describe the electrochemical reaction rate include the above-mentioned exchange current density, the transfer coefficient, the activation enthalpy, and the pre-exponential factor as well as the reaction order of the species involved. These parameters are not necessarily related to a single rate-determining step, as is often assumed in electrochemical theory. By investigating $i-\eta$ curves as functions of electrode potential, temperature, and concentration of the reacting species, insight may be gained into the reaction mechanism and microscopic transport processes (such as surface diffusion) that

determine the kinetic rate. This requires specialised electrochemical models, as discussed in Section 11.8.

Chemical reactions, too, may be characterised in a similar manner, following a strategy of effective kinetic parameters. When detailed knowledge of the reaction mechanism is lacking, the effective rate constants and other reaction-kinetic parameters can be determined by fitting a simplified kinetic model to the experimental data. For example, the steam-reforming conversion rate of CH_4 (reaction (15c)) may be expressed by the following empirical equation [6]:

$$dr_{CH_4}/dt = k_{CH_4} p_{CH_4}^{m_1} p_{H_2O}^{m_2} \exp(-E_{CH_4}/RT) \tag{16}$$

Different materials and designs will have different values for the parameters in Eq. (16). Depending on cell materials, the manufacturing process, and even the operating temperature, different values of m_1 and m_2 are possible [16–18]. Other rate expressions based on various kinetic models have also been proposed [19]. For realistic modelling, parameters that fit well with the desired systems should be used. Equation (16) represents the mass sink term for CH_4 in the CH_4 mass balance as given, in general form, by Eq. (1).

As Eq. (16) suggests, the effective rate constant strategy is particularly useful in the case of the anode fuelled by CH_4 because five or more gaseous species must be accounted for. Hydrogen is generated by steam reforming of CH_4 and by the forward process of the shift reaction $CO + H_2O \rightarrow CO_2 + H_2$. The backward process of the shift reaction and anodic hydrogen oxidation both consume hydrogen. The total rate of the mole change of H_2 is then

$$\mathrm{dr_{H2}/dt} = 3\mathrm{dr_{CH4}/dt} + \mathrm{dr_f/dt} - \mathrm{dr_b/dt} - \mathrm{dr_{H2}/dt(oxidation)} \tag{17a}$$

Here,

$$\mathrm{dr_f/dt} = k_1 p_{\mathrm{CO}} p_{\mathrm{H2O}} \tag{17b}$$

and

$$\mathrm{dr_b/dt} = k_1 \mathrm{K_{shift}} p_{\mathrm{CO2}} p_{\mathrm{H2}} \tag{17c}$$

where k_1 is a constant with dimensions of [kmol H_2 m^{-3} s^{-1} bar^{-2}]. From thermodynamics, the equilibrium constant of the shift reaction is given by

$$K_{shift} = \exp(-\Delta G^0_{shift}/RT) \tag{18}$$

where ΔG^0_{shift} is the standard Gibbs free-energy change of the shift reaction at temperature T and can be calculated from the standard Gibbs free-energy change at 298 K (ΔG^0_{298K}) and the standard enthalpy change at 298 K (ΔH^0_{298K}) with the help of heat capacities of reactant and product expressed as functions of temperature.

The rate of anodic hydrogen oxidation is proportional to the current density of hydrogen oxidation (i_{H2}). As discussed in Section 11.3, this current density according to the electrochemical model follows a Butler–Volmer-type equation (Eqs. (10a) and (10b)) with a concentration-dependent exchange current

density, i_o, which is specific for hydrogen oxidation. For gas-phase reaction calculations it is convenient to simplify Eq. (10b) in the form of an effective rate expression having an empirical rate constant, k_{H2}, reaction order, m_3, and activation energy, E_{H2}:

$$dr_{H_2}/dt(oxidation) = k_{H_2} p_{H_2}^{m_3} \exp(-E_{H_2}/RT) \tag{19}$$

Similarly, the rate of anodic oxidation of CO may be expressed by means of effective rate parameters:

$$dr_{CO}/dt(oxidation) = k_{CO} p_{CO}^{m_4} \exp(-E_{CO}/RT) \tag{20a}$$

The change in the CO concentration can then be written as

$$dr_{CO}/dt = dr_{CH4}/dt + dr_b/dt - dr_f/dt - dr_{CO}/dt(oxidation) \tag{20b}$$

Consequently, the rate of change of H_2O concentration is

$$dr_{H2O}/dt = dr_{H2}/dt(oxidation) + dr_b/dt - dr_f/dt - dr_{CH4}/dt \tag{20c}$$

At the cathode, too, effective rate expressions for oxygen reduction, if available, may be convenient, but the gas-phase mass balances are basically simpler than those at the anode. When current density is known, the rate of O_2 loss is

$$dr_{O2}/dt = i/4F \tag{21}$$

Assuming the current vector is everywhere transverse to gas flow direction, that is, perpendicular to the PEN element, Eq. (21) can be used to determine the variation of O_2 in an air channel. Similarly, if there is no current component parallel to the PEN element

$$dr_{H2}/dt(oxidation) + dr_{CO}/dt(oxidation) = i/2F \tag{22}$$

Because numerical error is inherent in modelling software, for exact mass balance, $i/2F - dr_{H2(CO)}/dt$ (oxidation) can determine $dr_{CO(H2)}/dt$ (oxidation), or dr_{H2}/dt (oxidation) + dr_{CO}/dt (oxidation) can determine $i/2F$. However, when a shift equilibrium reaction (15d) is achieved or assumed, the chemical equilibrium condition and Eq. (22) uniquely determine the sum of the rates of hydrogen and CO consumption. Therefore, separate rate parameter measurements for CO and hydrogen are not necessary. In fact, experience suggests that in most SOFCs the dominant anodic process is hydrogen oxidation, while CO is consumed by the shift equilibrium [10].

Similarly, if CH_4 is present and steam reforming is at equilibrium, chemical equilibrium conditions determine the rates of consumption of each fuel component uniquely for a given current production.

Combining the above rate equations and mass balances with the flow and thermal model equations presented in Section 11.2, detailed information about the variation of gas composition, fuel or oxidant utilisation, etc., in the flow channels may be generated.

The reactions presented thus far assume that the fuel mixture is CH_4/H_2O. The same approach would apply to other fuels such as H_2, CH_3OH, or dry CH_4 with corresponding changes in the reaction paths. If pure H_2 is used with a small amount of H_2O, the fuel composition and reaction mechanism are simplified. The number of experimental parameters and mathematical equations needed is reduced and the simulation is easier.

The equilibrium theory is very useful in addressing fuel processing issues whether or not equilibrium is attained. For example, with an internal reforming fuel cell the carbon forming reactions, decomposition of methane according to $CH_4 \rightarrow 2H_2 + C$, and Boudouard reaction, $2CO \rightarrow C + CO_2$, can be suppressed by providing a proper molar ratio of water to methane. For the external reforming subsystem, the theory can determine the optimal fuel-to-air ratio and operating temperature to maximise stack fuel (H_2 and CO) production while minimising equilibrium-predicted carbon formation. The equilibrium theory can also guide some cell design issues. Because steam reforming is an endothermic process, excessive cooling of the stack at the fuel inlet can occur with internal reforming. Nickel as an anode is known to be a good catalyst to promote cracking. A possible improvement is kinetic suppression of the cracking reaction using catalysts that are not as effective at promoting the cracking reaction. An alternative approach would use catalysts that promote electrochemical oxidation of hydrocarbons at lower operating temperatures. Figure 11.4 shows the equilibrium constant of the CH_4 steam reforming reaction as a function of temperature. Clearly, temperature has a significant effect on the resulting CH_4 content. CH_4 is stable against reforming at lower operating temperatures. Because suppression of steam reforming is also beneficial in full utilisation of the chemical energy of hydrocarbons, resulting in higher energy efficiency, considerable interest exists in direct electrochemical oxidation of natural gas and other hydrocarbons [20–22] in SOFCs.

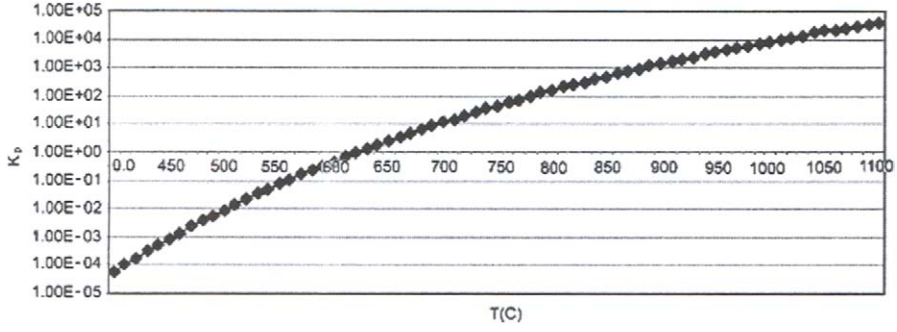

Figure 11.4 Equilibrium constant of methane steam reforming reaction as a function of temperature.

11.5 Cell- and Stack-Level Modelling

The coupled continuum-level electrochemical, flow, and thermal models are usually discretised in a finite element mesh [23,24]. When the necessary material properties, geometrical parameters, operating parameters, and boundary conditions are supplied, cell- and stack-level performance can be analysed. The combined models can determine the cell/stack voltage, the total current output, temperature distribution, species concentration, etc.

An important outcome of the combined models at the cell level is the cell efficiency, and at the stack level, the stack efficiency as well. The electrical efficiency of a cell and of the stack is defined as

$$\varepsilon_{el} = \text{electrical power output/chemical energy input per unit time} \qquad (23)$$

for the cell in question, and for the stack, respectively.

The electrical efficiency therefore depends to some extent on the definition of the fuel energy input and on whether power for gas pumping and the like is subtracted from the generated power. ε_{el} may be expressed in terms of current, voltage, etc., as follows:

$$\varepsilon_{el} = VI/(\Delta H dn/dt) \qquad (24a)$$

This can be considered the product of three additional fundamental efficiencies, namely the ideal or thermodynamic efficiency $\{\Delta G/\Delta H\}$, the voltage efficiency $\{V/E_0\}$, and the fuel utilisation $\{U_f\}$:

$$\varepsilon_{el} = VI/(\Delta H dn/dt) = \{\Delta G/\Delta H\}\{V/E_0\}\{U_f\} \qquad (24b)$$

The fuel utilisation, U_f, is the ratio of the delivered current to the stoichiometric current equivalent to the fuel flow rate:

$$U_f = I/(2F dn/dt) \qquad (24c)$$

The ideal efficiency $\Delta G/\Delta H$ may be considered a measure of the thermodynamic reversibility of the reaction and depends only on the operating temperature and fuel used. It is typically between 80 and 100%. The voltage efficiency and fuel utilisation, as well as the electrical energy efficiency, are useful measures for the success of the cell and stack design.

Another important figure of merit predicted by the combined model is the power density of a cell, or of the stack as a whole. The power density of a cell is usually defined on the basis of the cell or electrode area, that is

$$P_{cell} = I(\text{current}).V(\text{cell voltage})/A(\text{area}) \qquad (25a)$$

The power density of a stack is conveniently defined on the basis of stack volume:

$$P_{stack} = I(\text{current}).V(\text{stack voltage})/V(\text{stack volume}) \qquad (25b)$$

The cell- and stack-level models can improve understanding of the complex interactions between fluid dynamic, thermal, chemical, and electrochemical phenomena. The combined models can therefore help maximise efficiency or power density by optimising PEN element design, cell configuration, and stack architecture for a given set of operating conditions. Most SOFC modelling focuses on cell- and stack-level performance for exactly this purpose.

Cell-level models simulate the performance of a single cell, also called a unit cell. This is the repeating unit of a stack and consists basically of a PEN element, an interconnect layer, and a gas channel/current collector structure. The desired output is the current–voltage relationship, the temperature distribution, and the heat production in the cell. Cell-level models frequently treat the major cell components, the PEN element, the interconnect layer, and the gas flow, as two-dimensional (2-D) – having negligible thickness compared with the dimensions of the flow direction [12,25–27]. When the continuum flow/thermal/electrochemical model is treated as a 2-D model, calculations of heat production at any point of the cell plane (node of the 2-D model) can be simplified substantially. In such a 2-D cell model (or quasi-2-D stack model), heat generation may be determined by evaluating the change in gas composition between the inlet and exit conditions. The total energy (heat and work) delivered per unit time at each control volume (node) is simply

$$E_{\text{total}} = (\Delta H/\text{n}F)I \tag{26a}$$

where ΔH is the enthalpy of formation, representing the maximum chemical energy for the simplest $H_2 + 1/2O_2 \rightarrow H_2O$ reaction. Note that E_{total} is negative, in agreement with thermodynamic sign conventions for heat and work (heat positive when absorbed by, and work positive when performed on, the system). The heat generation, Q_{gen}, is then determined by subtracting from the total energy generation the electrical work delivered per unit time externally, i.e., the electric power:

$$P_{ex} = -I.V \tag{26b}$$

Therefore, the heat generated per unit time at each node is

$$Q_{\text{gen}} = (\Delta H/\text{n}F).I + V.I \tag{26c}$$

which is sometimes expressed in terms of the 'thermoneutral voltage' $V^{thn} = -(\Delta H/\text{n}F)$ as

$$Q_{\text{gen}} = (V - V^{thn}).I \tag{26d}$$

The expressions (26c) and (26d) for Q_{gen}, because they are derived from the overall change in thermodynamic state, account for all the various kinds of heat generation, including Joule (or ohmic) heating, heating due to polarisation, and entropic (TΔS) heat effects. The heat development at each node, $Q_{\text{gen(i,j)}}$, is

balanced by heat convection and conduction to and from adjacent nodes. Thus, all nodes in the 2-D model are thermally coupled to one another. Note, however, that in the 2-D model, the principal variable that determines the nonuniformity of heat generation, and therefore temperature, over the 2-D surface is the current I through each node (perpendicular to the 2-D plane). Applying the 2-D model to a planar stack with reasonably low in-plane electrical resistance (compared with the impedance of the electrochemical reaction), the variable V, the voltage at a given node, is relatively constant from node to node. Because the term $(V - V^{thn})$ is then also relatively uniform, the nonuniformity of I is the key to the temperature distribution. The principal cause of the nonuniformity of I, in turn, is the asymmetry of utilisation (hence of the local driving force, the local E_{eq}) imposed by the flow configuration of the planar cell.

In the 2-D cell simulation, as well as in simplified (quasi-2-D) stack-level simulations, it is usually assumed that each side of the electrode/interconnect is at equal potential over the whole 2-D plane of the cell. As mentioned above, this is justified because the ohmic voltage drop in the plane of the electrodes and interconnect layer is usually much smaller than the ohmic voltage drop across the electrolyte and the combined polarisation of the two electrodes. Nevertheless, in such a quasi-2-D stack model, individual fuel cells in the stack may have different cell voltages due to different temperature, fuel distribution, and other factors. However, the total current flow through each cell (integrated over the plane of the PEN elements and the gas flows) must be the same. The total stack output voltage is the sum of each individual cell voltage.

A true three-dimensional model [28–32] is necessary for a more accurate thermal analysis of a stack or for a detailed analysis of the temperature profile at the contact regions between PEN element, current collector/gas channel profiles, and the interconnect layer. In those cases, a more detailed heat source calculation is also needed. It is necessary to distinguish three different types of heat effects acting in specific components of the fuel cell: chemical, electrical, and electrochemical.

Chemical reactions (reforming and shift reactions) take place at the anode side, and chemical heat effects represent an important heat source (sink) term for the anode and the fuel channel.

The electrical heat effects are caused by resistance to current flow, which yields ohmic heating (also called Joule heating). Ohmic heating takes place throughout the solid structure wherever electrical current flows, for instance, from PEN element to interconnect layer. The total ohmic resistance can be decomposed into contributions from various cell components. If the component material has an ohmic resistivity γ_i (expressed in Ω m), the ohmic heat generated per unit volume of that computational region can be calculated from

$$Q_{ohm} = i^2 \gamma_i \tag{27}$$

where i is the local current density.

The electrochemical heat effect has two components: reversible or entropic heat effect (positive or negative, endothermic or exothermic), and irreversible

heat generation (always exothermic). Reversible heat generation is associated with the change of entropy occurring as a result of the electrochemical reaction. It is generated at the two electrodes in unequal amounts. In the case of hydrogen oxidation, the reversible heat generation at the anode per unit of projected area of the anode is

$$Q_{rev,a} = T(S_{H_2O} - S_{H_2} - S^*_{O^=} + 2S^*_{el})i/2F \tag{28a}$$

Here S_i is the entropy of the species i; that is, S_{O2} is the entropy of O_2, $S^*_{O^=}$ is the transported entropy of the oxygen ion, and S^*_{el} is the transported entropy of the electrons. The effect represented by Eq. (28a) is positive but relatively small [33]. The reversible heat generated at the cathode per unit projected area

$$Q_{rev,c} = T(S_{O^=} - \tfrac{1}{2}S_{O_2} - 2S^*_{el})i/2F \tag{28b}$$

is much larger and negative. Because the sum of the effects is equal to

$$Q_{rev,total} = T(S_{H2O} - S_{H2} - 1/2S_{O2})i/2F \tag{28c}$$

it follows that almost the entire entropic heat effect of the hydrogen oxidation reaction is released at the cathode. In some designs (with relatively thick electrolyte or thick anode) this may lead to significant temperature gradients, especially because cathode polarisation is usually dominant over anode polarisation, which further contributes to local heating at the cathode.

Conceptually, one can split the overall entropic effect, Eq. (28c), in two equal but opposite heat effects occurring at the two electrode-electrolyte interfaces. For example, the heat effect at the anode is

$$Q_{rev,a} = T(\tfrac{1}{2}S_{O_2} - S^*_{O^=} - 2S^*_{el})i/2F \tag{28d}$$

while that at the cathode is given by Eq. (28b). In that case, the overall reversible heat effect due to hydrogen oxidation (Eq. 28c) must be accounted for separately in the anode fuel gas channel. The advantage of introducing such a symmetric expression for the reversible heat effect is that in principle it allows taking into account heat development due to diffusion effects in the solid electrolyte upon current passage. However, in an SOFC these effects are minor compared with the Joule heating due to the ohmic resistance of the electrolyte included in Q_{ohm} (Eq. 27).

Irreversible heat generation due to the electrochemical reaction can be concisely represented by the local planar heat source for a two-electron reaction:

$$Q_{irr} = -(\eta_a + \eta_c)i/2F \tag{29}$$

Using an approximate electrochemical performance model, as discussed in Section 11.2, or a more detailed electrode-level model, as will be discussed in Section 11.8, the polarisation components can be estimated and the heat

generation calculated. In an approximate 3-D cell or stack model, it is customary to use a lumped electrochemical heat generation; that is, one assumes a uniform distribution of the reversible and irreversible heat generation over the respective electrode. Using a more advanced electrode-level model, the distribution of heat generation in the electrodes can be analysed, which may yield important information for structural stability of the electrodes and their interfaces with the electrolyte and the current collector/gas channel profiles.

The heat source terms discussed above are used in the energy balance equations of the flow and thermal models for both cell and stack simulations. To manage the computation cost, most simulations avoid the full CFD treatment of the flow. However, full CFD treatments provide more accurate and detailed information on the flow in an SOFC system. With increased computing power, more and more full CFD simulations are expected to appear.

Figure 11.5 shows sample cell modelling results: the steady-state temperature, current density, and species concentration distributions. As can be seen by comparison with Figure 11.2, the steady-state temperature distribution is quite different from that during the rapid startup.

Figure 11.6 shows the steady-state modelling results for a tubular SOFC design, as reported by Ferguson *et al.* [29]. Clearly, the characteristic operating

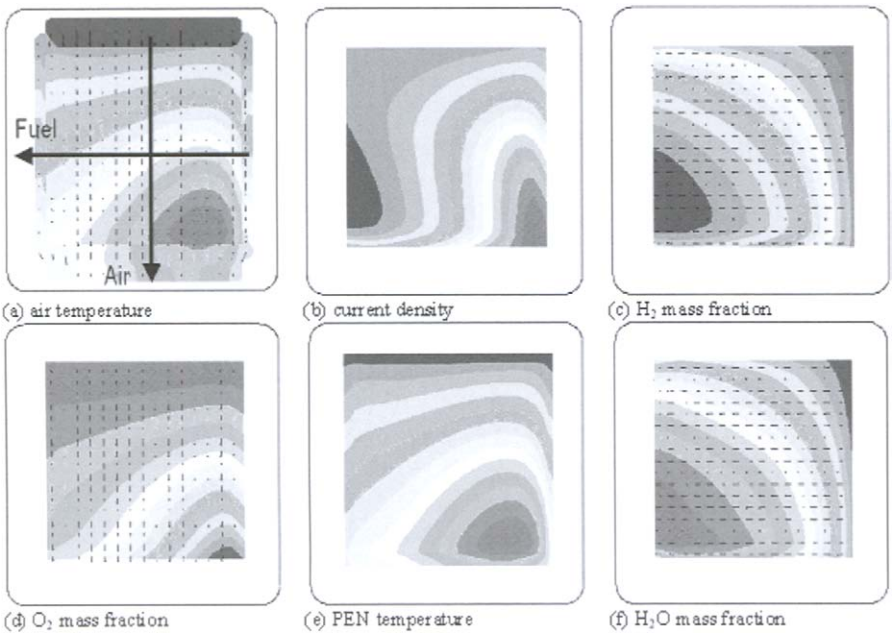

Figure 11.5 Sample results for planar SOFC in cross-flow configuration: a, air temperature, max. 899°C, min. 625°C; b, current, A/cm²: max. = 1.46, min. = 0.300; c, H_2 mass fraction, kg/kg: max. 0.0385, min. 0.00472 (CO distribution similar); d, O_2 mass fraction, kg/kg: max. 0.231, min. 0.182; e, PEN temperature, °C: max. 911, min. 643; f, H_2O mass fraction, kg/kg: max. 0.224, min. 0.0387 (CO_2 distribution similar).

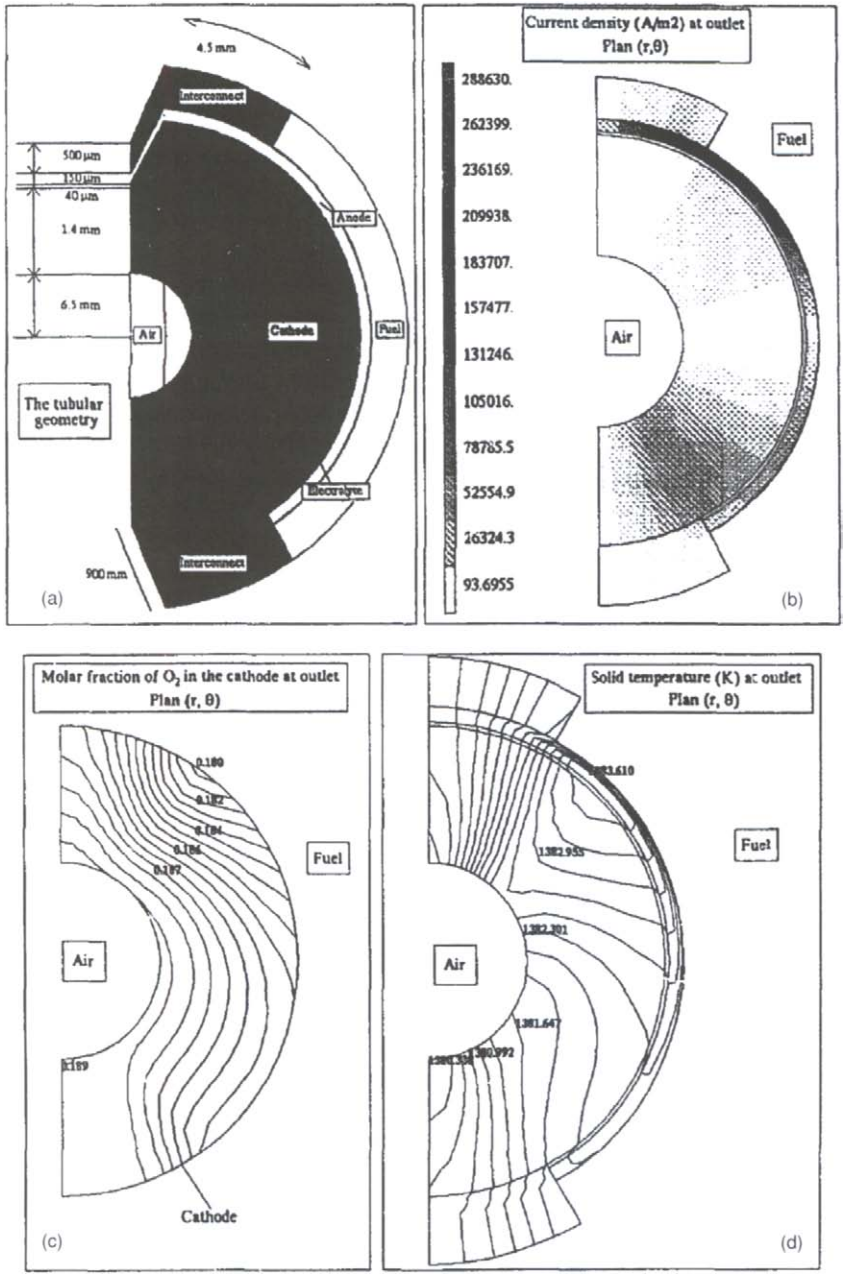

Figure 11.6 *(a) Three-dimensional section of a tubular design; (b) current density; (c) molar fraction of O_2; (d) temperature at the outlet section.*

properties for tubular designs are very different from that of planar SOFCs. Dedicated efforts are required for each individual design.

11.6 System-Level Modelling

In a system-level model, stack models are combined with models of system components including reformer, contaminant removal unit, compressors, topping or bottoming turbines, inverters, etc. The principal objective of system modelling is to determine the energy efficiency and heat/power ratio of the system. Such a model is also an excellent tool for making initial sketches of the system design and for initial sizing of components [14,34–38]. One example is the Excel spreadsheet model developed by Keegan *et al.* [14]. It combines models for gas preheater, reformer with recycle, stack, interface between stack and inlet gas, external reformer and exit gas, and combustor and uses heat balances and variable recycle ratio (with reformate composition as a function of recycle ratio) to evaluate (i) the overall system configuration and connectivity options, including various other recycle options, heat exchanger types, locations, and sizes; (ii) required energy transfer, resulting temperatures, and overall system efficiency, including pumping power and other parasitics, for the different proposed system designs; (iii) subsystem requirements associated with specific selected configurations, including required stream mass flows and allowable branch pressure drops; (iv) system performance at various load conditions; and (v) dynamic system performance during startup to determine additional constraining requirements, including allowable thermal mass and required heat transfer. The model also evaluates the system cycle efficiency, that is, the overall system performance as a function of the system start-up and shut-down cycling.

Another example is the systematic analysis undertaken by Palsson *et al.* on combined SOFC and gas turbine cycles [36]. In combination with a robust and accurate 2-D SOFC model, the system-level model attempts to provide an unbiased evaluation of performance prospects and operational behaviours of such systems. The 2-D SOFC model was integrated into a process simulation tool, Aspen Plus^{TM}, as a user-defined model, whereas other components constituting the system are modelled as standard unit operation models. Parametric studies can be carried out to gain knowledge of stack and system behaviour such as the influence of fuel and air flow rate on the stack performance and the mean temperature and the effects of cell voltage and compressor pressure on the system efficiency. The pressure ratio is shown to have a large impact on performance and electrical efficiencies of higher than 65% are possible at low-pressure ratios.

Extensive system modelling for SOFC systems has been carried out and published by Winkler *et al.* [37,38]. Their publications cover the methodology of system modelling as well as the effect of hardware design variations on efficiency and cost of integrated SOFC-GT hybrid systems. The market acceptance ultimately depends on the system cost, which is influenced by the process design, hardware design, production (materials and handling), and market (production quantity). Based mainly on the thermodynamics, the process design examines

issues such as the choice of heat engine and the integration of heat engine and heat exchangers. The hardware design examines the geometric effects on the system cost through its effects on the power density, thermal insulation, and the wall of the pressure vessel. Such analysis provides valuable information for design optimisation.

These and other system modelling analyses show how strongly system characteristics such as efficiency depend on accurate input data for the electrochemical model used in simulating stack performance. On the other hand, these studies also show the strong effect of turbine operating parameters (e.g., pressure ratios and maximum allowable temperature) on the system performance. Such studies clarify that the ultimate design of the stack and the required accuracy of stack modelling are best determined after preliminary system design studies have been performed using rough stack, reformer, and turbine models.

11.7 Thermomechanical Model

Avoiding thermomechanical failure is critical to the applications of the SOFC technology. SOFCs are produced by processing at elevated temperatures. As the cells are cooled to room temperature, stresses due to mismatch in coefficients of thermal expansion (CTEs) are developed. Additional residual stresses develop in the stack during the assembly and sealing process. The factors that affect the magnitude of the stresses include (i) differences in CTEs of the material parts, (ii) the differential between stress-free (processing) temperature and operation temperature, (iii) elastic constants of the components, and (iv) the thickness of the cell components. Because the cell thickness is much less than the lateral dimensions, the elasticity problem may be approximated as 2-D and the state of stress is thus biaxial. For the state-of-the-art PEN materials, cathode (LSM) and electrolyte (YSZ) have similar CTEs, while the CTE of the anode (Ni + YSZ) is higher. Thus, when cooled from a high temperature, stresses in the electrolyte and the cathode would tend to be compressive, while stresses in the anode would be tensile. In an anode-supported cell, the tensile stress can cause a delamination crack between the anode and the electrolyte.

The residual stress in a cell when cooled from stress-free temperature to room temperature can be calculated [39]:

$$\sigma_1 = (\beta_2 - \beta_1)E_1\Delta T/[1 + h_1E_1/h_2E_2] \tag{30}$$

where β is the thermal expansion coefficient, ΔT is the change in temperature, h is the layer thickness, and E is the biaxial modulus. The subscripts '1' and '2' denote two neighbouring layers of the cell. From Eq. (30) it can be seen that thin layers suffer higher residual stresses than thick layers. In the anode-supported cell, the electrolyte has a much higher residual stress than the anode. Fortunately, the electrolyte is strong against compressive stresses. For the anode, the tensile stress is a concern. Assuming $\Delta T = 1000\,K$, $\beta_2 - \beta_1 = 1.7 \times 10^{-6}/°C$, $E_2 = 200\,GPa$,

and $h_1/h_2 = 60$, the residual stress is about 6 MPa. For cathode-supported cells, however, the anode residual stress could be one order of magnitude higher and is very undesirable. The anode residual stress is the highest in the electrolyte-supported cells.

When temperature distribution in the cell structure is known, the finite-element structure model can analyse the thermal stresses. The thermal stresses dictate the process of heating and cooling required in SOFC applications. Thermal stresses also dictate how uniform the temperature should be in steady-state operations. Modelling results indicate that temperature gradient makes the largest contribution to overall stress. Moreover, it is important to maintain a uniform temperature gradient along the cell in minimising the anode/electrolyte/cathode stress. Figure 11.7 demonstrates the dramatic reduction in stress going from a parabolic temperature distribution to uniform temperature gradient.

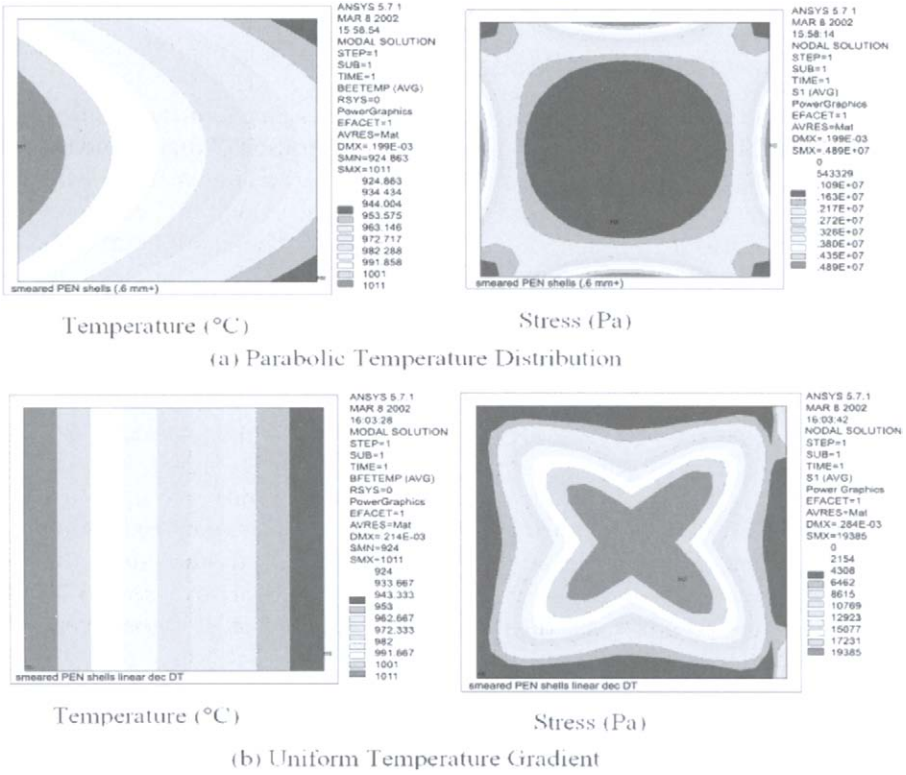

Figure 11.7. Effect of temperature profile on SOFC stress.

The probability of failure under stress σ can be calculated from the Weibull function:

$$W = 1 - \exp[-(\sigma/\sigma_0)^m] \tag{31}$$

The Weibull parameter m and the characteristic stress σ_0 are material-specific parameters.

Mechanical failure can be caused by various mechanisms. As discussed, the electrolyte and the cathode are subjected to compressive stresses due to thermal mismatch. For thin-film coating under compressive stress, a common failure mode is buckle-driven delamination, or blistering [40]. The failure entails the film first buckling away from the substrate in some small region where adhesion is poor or nonexistent. Buckling then loads the interface crack between the film and the substrate, causing it to spread. Another failure mode of the fuel cell structure is thermal shock spalling. During thermal cycling, biaxial tensile residual stress can develop in and spall the surface layer. The spall depth and the time elapse can also be analysed with the finite-element method once the temperature gradient is known.

The mechanical strength of a metallic interconnect such as stainless steel 430 decreases significantly at elevated temperatures. Modelling results indicate that the portion of the interconnect near the fuel cell edge often suffers from high tensile stress. Therefore, optimising designs and operating conditions to reduce the interconnect stress is also a focus of the modelling activity.

The thermal stress consideration also limits the design and material choice for the seal. The seal is responsible for the gas-tight separation of the air and the fuel gas chambers and air manifold from the fuel electrode and fuel manifold from the air electrode porosities. In addition, to prevent gas crossover the sealant should be strong and stiff so that stacks are mechanically stable, can be handled, and can withstand pressure differences during operation. On the other hand, the sealant must be soft enough to reduce mechanical stresses during fabrication and operation. Moreover, the requirement of chemical compatibility with other cell components (electrolyte, electrode, interconnect) as well as stability in both oxidising and reducing gas atmospheres should also be satisfied. These considerations affect whether the design should be rigid glass seal; flexible, glass-free, compression seal; or a combination of the two [41,42].

Dimensional changes of components may arise due to a change in temperature. Nonstoichiometric oxides exhibit an expansion behaviour depending on oxygen stoichiometry due to reduction or oxidation upon changes in oxygen partial pressures. Interconnect and electrolyte are exposed to different oxygen partial pressures at the anode and cathode side, respectively. An expansion behaviour depending on oxygen nonstoichiometry can therefore lead to different expansions on each side of the interconnect. Bending and mechanical failure may result. As a simple one-dimensional example, the steady-state thermal stress, σ, in an infinitely wide, free plate subject to a temperature distribution, T(z), which varies only in the direction of the thickness, z, can be expressed as [43]

$$\sigma_x = \sigma_y = -\frac{\beta E}{1-\nu}\left\{ T + \frac{1}{2d}\int_{-d}^{d} T dz + \frac{3z}{2d^3}\int_{-d}^{d} T z dz \right\} \tag{32}$$

where β is the CTE, E is the Young's modulus, ν is the Poisson's ratio, and d is the half-thickness of the plate. Assuming that the lattice expansion-induced strain can be treated the same way as the thermal strain, βT, Eq. (32) can be recast into a stress–isothermal strain relation. The experimental data for the isothermal expansion characteristics can then be used to obtain the nonstoichiometry-induced strain. Consequently, the isothermal stress due to nonstoichiometry can be determined. Delamination will occur if the elastic energy release rate by crack formation exceeds a critical value where the critical value is an interface property and must be determined experimentally. Alternatively, mechanical failure occurs if the thermal stress exceeds a certain value.

11.8 Electrochemical Models at the Electrode Level

Electrode-level models describe the performance of SOFC electrodes in detail. They take into account the distribution of species concentrations, electric potential, current, and even temperature in the electrode. Their purpose is to (i) interpret the performance (polarisation curve) of electrodes in terms of rate-limiting resistances such as kinetic (activation), mass transfer, and ohmic resistance; and (ii) predict the local polarisation in full-scale cell and stack models.

To predict the local polarisation in a full-scale cell or stack at any point, its dependence on composition, pressure, and temperature of the gas flowing in the gas channel contacting the electrode must be known. In a large cell, these bulk gas properties vary from one point to the next. Electrode polarisation or overpotential – the difference between the local potential of the electrode under load and the potential at open circuit (equilibrium potential) – is also a local quantity because it depends not only on the bulk gas composition but also on the current density. In a large cell the current is usually distributed nonuniformly, as discussed in Sections 11.2–11.5. Similar to Eq. 7, one can express the local cell voltage under load, i.e., when current is passed, as the thermodynamic cell potential minus three loss terms: the ohmic loss, the cathode polarisation, and the anode polarisation:

$$V(i) = \mathrm{E_{eq}} - iR_i - \eta_\mathrm{C} - \eta_\mathrm{A} \tag{33}$$

As discussed in Section 11.2, the total polarisation of each electrode consists of two contributions, activation polarisation (due to electrode kinetic resistance) and concentration polarisation (due to mass transfer resistance), so

$$\eta_\mathrm{C} = \eta_\mathrm{Ca} + \eta_\mathrm{Cc} \quad \text{and} \quad \eta_\mathrm{A} = \eta_\mathrm{Aa} + \eta_\mathrm{Ac} \tag{34}$$

For cell- and stack-level modelling it is necessary to have reliable values of the total polarisation of cathode, η_C, and anode, η_A, as a function of local bulk gas composition, pressure, and temperature, as well as the local current density.

In principle, one could make a large set of measurements of cathode and anode polarisations in a small-size cell with a reference electrode (three-electrode cell) and express the total polarisation as a function of local bulk gas composition, pressure, temperature, and current density. The essential condition is that the small-size cells ('button cells') use very little fuel gas and oxidant gas, so that the measured polarisation is representative for the bulk gas composition, pressure, and temperature at a given current level. The cell then functions as a differential reactor that provides data for the cell- and stack-level (integral reactor) modelling. Although small-size cell data are obviously useful and many such measurements are made, the effort implied in a full 'polarisation mapping' of this kind for each electrode is usually prohibitive. Moreover, the results are valid only for the range over which the operating parameters are varied and for the electrode–electrolyte assembly microstructure and configuration used in the small-size cell.

In lieu of an experimental 'map' of polarisation, it is often desirable to have an electrode model that provides reliable predictions of polarisation of either electrode over a wide range of operating and structural variables. This is the first purpose of the electrode model. But, conversely, to be a good predictor the model should be capable of interpreting available polarisation data for well-defined conditions, that is, for small cells at low utilisation of fuel or oxidant. Thus, the second purpose of an electrode model is to enable a more efficient process of collecting, correlating, and interpreting polarisation data. The electrode model is capable of extracting the kinetic and mass transfer (diffusion) resistance information by fitting small-size cell polarisation data. It provides these resistance characteristics in a form suitable as input to full-scale cell and stack models.

An electrode model is especially advantageous if it can be used to relate the kinetic and mass transfer resistance to electrode geometry and microstructure; for instance, to thickness, porosity, pore or particle size, contact areas of phases, and/or grain size of electrode and electrolyte materials. A well-tested and validated electrode model, therefore, may serve to assist in the design of optimised electrode structures or electrode/electrolyte interfaces to minimise polarisation loss.

11.8.1 Fundamentals and Strategy of Electrode-Level Models

The objective of an electrode model is to analyse the point-to-point distribution of the reaction in an SOFC electrode, leading to current, potential, and species concentration distributions. The result of the analysis is a prediction of the polarisation of the electrode due to (i) kinetic resistance, (ii) mass transfer resistance, and (iii) ohmic resistance.

The analysis includes a whole set of material properties and structural parameters. In principle it is based on the same fundamental laws used in full-scale cell analysis. Thus, mass transfer is subject to mass balances (Eqs. (1), (2)), heat flow to energy balances (Eqs. (5), (6)), and fluid flow to Eqs. (3), (4), but it is usually negligible in the pores of the electrodes. In addition, current flow is

subject to the electrical conservation equation (under assumption of electroneutrality):

$$(\nabla \cdot i) = 0 \tag{35}$$

where i is the current density vector. This yields for the potential distribution Laplace's equation:

$$(\nabla^2 \Phi) = 0 \tag{36}$$

with the appropriate boundary conditions for conducting and nonconducting boundaries. Equations (35) and (36) may be applied separately to the ionic current and its associated electric potential, respectively, and to the electronic current and its associated electric potential. This is very helpful in formulating the electrochemical rate at each point of the electrode/electrolyte interface by equating the local potential difference $\Phi_{\text{electronic}} - \Phi_{\text{ionic}}$ with the total overpotential $\eta = V - E_{eq}$ at that point of the interface. This coupling of the potential distribution, which obeys Eq. (36), with the electrochemistry and thermodynamics of the electrode reaction leads to a generalised potential balance equation, of which Eq. (7) is a specific form valid for thin planar cells.

In a similar manner, the species mass balance equations, Eqs. (1), (2), may be coupled with the electrochemical rate at each point of the reaction zone (at or near the TPB). In the continuum-level modelling discussed in Section 11.2, the concentration polarisation of the electrode, η_{conc}, was related to a limiting current of the reactant, e.g., Eq. (9). A more fundamental and general expression for the concentration overpotential (the term 'overpotential' denotes exclusively the local polarisation) at any point of the electrode reaction zone is the so-called Nernst equation; for example

$$\eta_c = RT/nF \ln[(c_{r,\text{electrode}}/c_{r,\text{bulk}})/(c_{p,electrode}/c_{p,bulk})] \tag{37}$$

This is valid for a simple electron transfer reaction $r + ne^- = p$ but may easily be generalised. Because the fundamental mass balance equations, Eqs. (1), (2), in the absence of convection become diffusion equations, the solution of the diffusion equations for species r and p yields the concentration overpotential, η_c, at any point of the reaction zone.

Once the local concentration overpotential is known, the activation overpotential, η_a, is obtained by subtracting η_c from total η. The local activation overpotential is the actual driving force of the electrochemical reaction. It is related to the local current density at any point of the reaction zone by an electrochemical rate equation such as the Butler–Volmer equation (Eq. (10a)). Therefore, the rate equation, the Nernst equation (Eq. (37)), and the potential balance in combination couple the electric field with the species diffusion field. In addition, the energy balance applies also at the electrode level. Although this introduces another complication, a model including a temperature profile in the electrode is very useful because heat generation occurs mainly by electrochemical reaction and is localised at the reaction zone, while the

strong temperature sensitivity of properties like electrolyte conductivity and electrode kinetics may skew the reaction distribution from that expected in isothermal operation.

Thus, even at the electrode level the interactions between electrochemical reaction, mass transfer, ionic conduction, and heat transfer yield a very complicated set of equations. Of course, this has given rise to many attempts to use simplified models wherever possible. Some of these are summarised below. Several are based on an assumption of one or more dominant rate-controlling resistances, for instance, mass transfer or ohmic resistance or neglect of coupling conditions that complicate the reaction distribution. Others introduce linearised electrode kinetics and neglect mass transfer resistance. Of course, these simplifying assumptions must be validated.

Validation by fitting empirical polarisation curves is helpful, especially if the objective is input for full-scale performance models. But it is of limited value if the parameter space of the fitted curves is restricted, especially when the objective is optimisation of electrode design. Benchmarking results of simplified models against a set of more complete model equations is also helpful but limited by uncertainty about some important coupling conditions. The important role of the reaction mechanism in determining kinetic rates has been recognised early and has led to specialised electrode modelling focused on this aspect of the electrode process. In addition, it has recently been realised that computational studies of the electrochemical reaction steps may contribute to greater insight in those aspects of the electrochemical rate process that are specific for the SOFC.

The following summarises a few types of simplified electrode models proposed in the literature.

11.8.2 Electrode Models Based on a Mass Transfer Analysis

If the reaction kinetics of the electrode is assumed to be very rapid, mass transfer and ohmic resistance are the dominant resistances. Assuming a reaction zone that coincides with the electrode-electrolyte interface, the diffusion fluxes in stationary operation can be expressed simply in terms of bulk gas partial pressures and gas-phase diffusivities. This is illustrated schematically in Figure 11.8, which compares anode- and cathode-supported cell designs for the simple case of a H_2/O_2 fuel cell. The decrease in concentration polarisation at the cathode, η_{Cc}, is obvious in the case of an anode-supported cell, while the model shows that concentration polarisation at the anode, η_{Ac}, is relatively insensitive to anode thickness. The advantage of the mass transfer-based approach is that analytical expressions are obtained for the polarisation behaviour. These are rather simple if activation overpotential is excluded but may still become elaborate in the case of an internally reforming anode where a number of reactions (discussed in Section 11.3) may occur simultaneously within the pores of the anode.

In further development of this model, a finite reaction zone may be introduced and activation overpotential added to the polarisation [44–47]. Kinetic resistance is believed to be particularly important for the cathode (η_{Ca} is

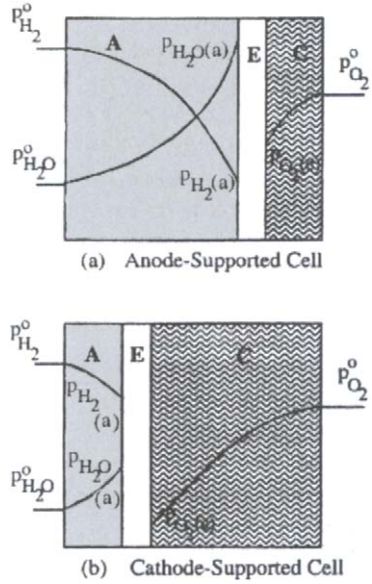

Figure 11.8. Schematic diagram of (a) anode- and (b) cathode-supported SOFCs [47].

not negligible); however, this adds further parameters of uncertain magnitude to the polarisation expressions and detracts from their original conciseness. The simplicity of the mass-transfer-based approach makes it attractive as a first-order approach in scale-up modelling [5,48,49] because it is axiomatic in practice that a good fuel cell electrode should have rapid kinetics. However, for analysis of transients other simplified models may be preferable, and for optimisation of electrode microstructure other specialised models may be equally suitable.

11.8.3 One-Dimensional Porous Electrode Models Based on Complete Concentration, Potential, and Current Distributions

Simplified models that do not make *a priori* assumptions about one or more dominant resistances are often of the 1-D macrohomogeneous type. The 1-D assumption is similar to that in mass transfer-based models. The assumption of macrohomogeneity, based on work by Newman and Tobias [50], has proven useful in battery and fuel cell electrode modelling. It implies that the microstructure of the electrode is homogeneous at the level of the continuum equations governing mass transfer, heat transfer, and current conduction in the electrode (Eqs. (1)–(7) and (33)–(37)). This type of model can exploit solutions available in chemical reaction engineering practice and has been elaborated by several researchers in that field [51–55].

Mathematically, the three phases, the solid electrocatalyst, the solid electrolyte, and the gas, are assumed to be present simultaneously at each point. The microstructure of the electrode, which produces the interface between the

three phases, is represented by a volumetric interfacial reaction area (designated by a_m) with a meaning similar to that of the dimensionless interfacial area factor a in Eq. (10b). Across the interface represented by a_m, the electrochemical reaction takes place, generating electronic and ionic current fluxes and their associated potentials, as discussed under Eqs. (35) and (36). The species concentration and ionic or electronic current fluxes are projected with respect to the macrohomogeneous electrode cross section. This implies that the volume fractions of electrocatalyst, electrolyte, and gas-filled pores are necessary structural parameters, in addition to a_m.

The simplification inherent in the 1-D macrohomogeneous model is that of the microstructure. For the model to be useful in optimising electrode microstructure, the parameter a_m must be related to microstructural characteristics such as pore size and porosity. There are various techniques available from percolation theory to accomplish this and relate a_m and other model parameters to empirical pore-size distribution and total pore volume.

One of the advantages of the 1-D macrohomogeneous approach is that complete diffusion, reaction, and potential profiles are obtained, which is advantageous when the relative rates of competing reactions (for example, anodic oxidation of H_2 compared with direct anodic oxidation of CO or even direct anodic oxidation of CH_4) are compared. Another advantage is that no a priori assumption is made about the location of the reaction zone. The zones of maximum reaction are identified from the current and potential profiles and can be correlated with structural characteristics and operating variables. Finally, the very general formulation of the fundamental equations makes it possible to use dimensional analysis as a guide in correlating results and fitting against experimental data [55].

To illustrate the detailed nature of results from such a model, Figure 11.9 shows the distribution of local overpotential in the pore of an internally

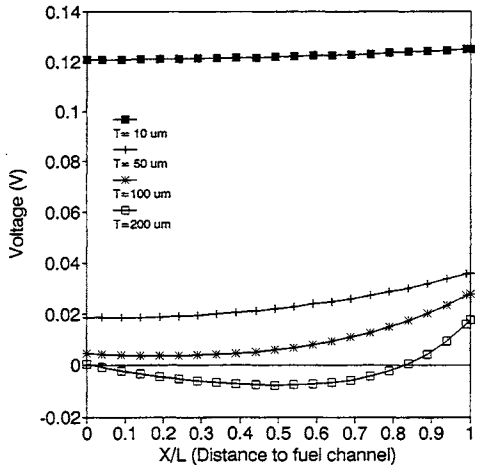

Figure 11.9 Distribution of local overpotential at the pore wall of an internally reforming anode, with fuel gas containing 33% CH_4, 66% H_2O, balance CO and H_2, at 0.2 A/cm^2 [51].

reforming anode as a function of pore size. In extremely wide pores, the overpotential is negative over a large part of the pore wall (away from the interface with the electrolyte), indicating that the electrochemical process may be reversed away from the interface and hydrogen generation occurs not only by reforming but electrochemically if pore dimensions are not optimised.

11.8.4 Monte Carlo or Stochastic Electrode Structure Model

A third distinct type of electrode model developed in response to the need for modelling the composite structure of SOFC electrodes more accurately is the Monte Carlo, or stochastic structure, model. This model is based on a random number-generated 2- or 3-D structure of electrode particles, electrolyte particles, and holes (for gas pores). It has been shown to represent the composite conductivity quite well and may be able to model polarisation behaviour adequately [56–58]. This is of interest because microstructure, and in particular hard-to-control variations in local microstructure, may have an important effect on overall polarisation, perhaps more so than the intrinsic kinetic characteristics measured at an 'ideal' interface.

The Monte Carlo-type electrode model is also called the particle connectivity model because its physics is straightforwardly based on Kirchhoff's law for an electrical network, with particle resistance and interconnection resistances defined by a set of rules to mimic the current flow and electrochemical current generation within the microstructure. The electrochemical process is considered to take place with a constant resistance in agreement with intuitive notions about the mechanism. Variants of this concept attach correlated values to the resistances in the network to model polarisation more closely according to a percolation concept of active sites and passive connections [59]. Other specialised types of electrode models are mentioned briefly below.

11.8.4.1 Electrode or Cell Models Applied to Ohmic Resistance-Dominated Cells

These models start from solving Laplace's equation (Eq. (36)) with appropriate boundary conditions, sometimes including polarisation. The most important application is the correct design of test cells with reference electrodes because small deviations in reference electrode placement may cause appreciable deviations in polarisation readings [60–63].

11.8.4.2 Diagnostic Modelling of Electrodes to Elucidate Reaction Mechanisms

Because the electrode kinetics of both anode and cathode and their dependence on microstructure are so important for performance, much attention has been given to elucidating reaction mechanisms based on independent electrochemical measurements (usually with respect to a reference electrode). AC impedance measurements are particularly favoured. The interpretation of these measurements requires specialised models that reflect in part the hypothesised kinetics and in part the electrode structure. It seems certain that

eventually the results will be integrated with both macro- and molecular modelling [64–69].

11.8.4.3 Models of Mixed Ionic and Electronic Conducting (MIEC) Electrodes

These specialised electrode models usually consider the MIEC electrode in combination with the electrolyte and focus on correlating performance with the semiconductor characteristics of the electrode (and sometimes electrolyte) [70–72]. Recent modelling of oxygen reduction and oxygen permeation at perovskite electrodes includes both MIEC effects and classical diffusion-type analysis [73–75].

11.9 Molecular-Level Models

Molecular-level SOFC models aim to understand (i) the kinetics of the reaction at the interface between electrode and electrolyte, (ii) the conduction process in the electrolyte, and (iii) the conduction process in the electrodes. Catalytic activity at TPB, activation energy for oxygen ion transport, and surface exchange current are application examples for such models.

Within the last two decades, enormous progress has been achieved in the ability to calculate the structures, the properties (e.g., thermodynamic, mechanical, transportation properties), and the reactivity of solids starting from atomistic approaches. The molecular-level models can be classified into three categories.

- *Empirical interatomic potential models.* Such simulations start from a given effective potential that describes the interatomic forces in a system of atoms using essentially classical techniques. The simulation algorithms are based on static minimisation methods to calculate the structural configuration of the lowest potential energy. One popular approach is the molecular dynamics method. Classical molecular dynamics can use the simple interatomic potential as well as kinetic energy to simulate fast diffusion and high-temperature properties as well as other material properties. Molecular dynamics has been performed to investigate the grain boundary phenomena in cubic zirconia at constant temperatures up to 2673 K with a system of 1920 atoms [76]. Simulations indicate that the interfaces between perfect zirconia crystals are sources of resistance in these ionic conducting systems. Another approach is Monte Carlo methods, computing random changes in the structure with results accepted or rejected on the energy criterion. Monte Carlo methods are suitable to treat disordered systems and, for example, the vacancy distribution and ion motions in heavily doped, fast ionic conducting fluorite oxides such as CeO_2 [77].
- *Quantum mechanical electronic structure calculations, or the ab initio methods. Ab initio* methods are based, at some level of simplification, on the

self-consistent solution of the Schrödinger equation for a cluster (up to about 100) of atoms and a set of (usually periodic) boundary conditions [78–80]. *Ab initio* calculations can be useful in furthering the understanding of the electrode process. For example, the computed barrier to desorption of H_2O_{ad} on Ni may be used to see whether it is the rate-determining step. Calculations can also be used to understand the reaction of H_{ad} and O_{ad}, H_{ad} and OH_{ad} as well as adsorption and diffusion of H, OH, and H_2O on the YSZ. This could be very useful in finding new catalysts capable of providing a current orders of magnitude larger than Ni as only a very small fraction of H_{ad} on Ni participates in the oxidation reaction [79,80]. By effectively eliminating the need for the self-consistent iterative process, accurate and robust *ab initio* molecular dynamics are now available, and simulations for systems of more than 100 atoms can be performed in a single CPU [81,82].

- *Hybrid techniques.* These use, for example, quantum mechanical techniques or their simplified variants to provide the effective potentials needed for the simulation of interatomic forces [83]. The computational efficiency and accuracy of the hybrid methods fall between the *ab initio* methods and the empirical methods.

With the improvement in hardware and software tools, the *ab initio* electronic structure calculations will gain importance because they can deal with increasingly complex systems and yield higher precision in the result. Along with this trend, the hybrid techniques will grow in relevance. It is expected that the hybrid methods will play an important role in the molecular-level modelling of SOFCs in the near future.

11.10 Summary

Modelling of SOFCs is advancing at a rapid rate, facilitating quick predictions of SOFC performance at a number of levels, and aiding the design of SOFC systems. Macroscopic flow and thermal models are the best known and have followed from straightforward chemical engineering principles of mass and energy balance. At the nanoscale of atoms and molecules, predictions of material behaviour and of interface interactions are also becoming possible. Most significant advances are now taking place in the understanding of complex composite structures of electrodes and three phase boundaries. Ultimately these should lead to predictions of cell behaviour which at present are measured empirically and inserted into stack models. Stack modelling has advanced to the point where acceptable start-up rates can be predicted and where overall performance can be optimised. The integration of these stacks into complete systems can also be predicted with some precision, leading to new design possibilities for hybrid SOFCs. In the immediate future, it is anticipated that models which combine the macroscopic and atomistic approaches will develop rapidly.

References

[1] E. Arato, P. Costamagna and P. Costa, *Chem. Biochem. Eng. Q.*, **8**(20) (1994) 85.

[2] J. C. Tannehill, D. A. Anderson and R. H. Pletcher, *Computational Fluid Mechanics and Heat Transfer*, 2nd edition, Taylor and Francis, Washington, DC, 1996, Ch. 5.

[3] R. J. Boersma and N. M. Sammes, *J. Power Sources*, **63** (1996) 215–219.

[4] E. Achenbach and U. Reus, in *Solid Oxide Fuel Cells VI*, eds. S. C. Singhal and M. Dokiya, The Electrochemical Society Proceedings, Pennington, NJ, PV99-19, 1999, pp. 1125–1134.

[5] J. Yuan, M. Rokni and B. Sunden, in *Solid Oxide Fuel Cells VI*, eds. S. C. Singhal and M. Dokiya, The Electrochemical Society Proceedings, Pennington, NJ, PV99-19, 1999, pp. 1099–1108.

[6] H. Yakabe, T. Ogiwara, I. Yasuda and M. Hishinuma, in *Solid Oxide Fuel Cells VI*, eds. S. C. Singhal and M. Dokiya, The Electrochemical Society Proceedings, Pennington, NJ, PV99-19, 1999, pp. 1087–1098.

[7] M. Suzuki, A. Hirano, T. Ioroi, Z. Ogumi and Z. Takehara, in *Solid Oxide Fuel Cells V*, eds. U. Stimming, S. C. Singhal, H. Tagawa and W. Lehnert, The Electrochemical Society Proceedings, Pennington, NJ, PV97-40, 1997, pp. 1359–1367.

[8] P. Costamagna and E. Arato, in *Solid Oxide Fuel Cells V*, eds. U. Stimming, S. C. Singhal, H. Tagawa and W. Lehnert, The Electrochemical Society Proceedings, Pennington, NJ, PV97-40, 1997, pp. 1339–1348.

[9] M. A. Khaleel, K. P. Recknagle, Z. Lin, J. E. Deibler, L. A. Chick and J. W. Stevenson, in *Solid Oxide Fuel Cells VII*, eds. H. Yokokawa and S. C. Singhal, The Electrochemical Society Proceedings, Pennington, NJ, PV2001-16, 2001, p. 1032.

[10] EG&G Services, Parsons, Inc., and Science Applications International Corporation, in *Fuel Cell Handbook*, 5th edition, U.S. Department of Energy, National Energy Technology Laboratory, Morgantown, WV, 2000.

[11] I. Riess, *J. Electrochem. Soc.*, **128** (1981) 2077–2081.

[12] C. Milliken, S. Guruswamy and A. Khandkar, *J. Electrochem. Soc.*, **146** (1999) 872–82.

[13] H. L. Tuller, J. Schoonman and I. Riess, *Oxygen Ion and Mixed Conductors and their Technological Applications*, Kluwer Academic, Dordrecht, 2000.

[14] K. Keegan, M. Khaleel, L. Chick, K. Recknagle, S. Simner and J. Deibler, in *Proceedings of the 2000 Society of Automotive Engineers Congress*, 2002-02-0413, 2002.

[15] J. W. Kim, A. V. Virkar, K. Z. Fung, K. Metha and S. C. Singhal, *J. Electrochem. Soc.*, **146** (1999) 69–78.

[16] T. Tojo, T. Atake, T. Mori and H. Yamamura, *J. Chem. Thermodynamics*, **31** (1999) 831–845.

[17] S. Srinivasan, R. Mosdale, P. Stevens and C. Yang, *Annu. Rev. Energy Environ.*, **24** (1999) 281–328.
[18] S. Nagata, A. Momma, T. Kato and T. Kasuga, *J. Power Sources*, **101** (2001) 60–71.
[19] K. Ahmed and K. Foger, *Catalysis Today*, **63** (2000) 479–487.
[20] E. P. Murray, T. Tsai and S. A. Barnett, *Nature*, **400** (1999) 649–651.
[21] S. Park, J. M. Vohs and R. J. Gorte, *Nature*, **404** (2000) 265–267.
[22] T. Hibino, A. Hashimoto, T. Inoue, J. Tokuno, S. Yoshida and M. Sano, *Science*, **288** (2000) 2031–2033.
[23] R. D. Cook, D. S. Malkus and M. E. Plesha, *Concept and Applications of Finite Element Analysis*, 3rd edition, John Wiley, New York, 1989.
[24] J. M. Fiard and R. Herbin, *Comput. Methods Appl. Mech. Eng.*, **115** (1994) 315–338.
[25] C. G. Vayenas, P. G. Debenedetti, I. Yentekakis and L. L. Hegedus, *Ind. Eng. Chem. Fundam.*, **24** (1985) 316–324.
[26] S. Ahmed, C. McPheeters and R. Kumar, *J. Electrochem. Soc.*, **138** (1991) 2712–2718.
[27] P. Costamagna and K. Honegger, *J. Electrochem. Soc.*, **145** (1998) 3995–4007.
[28] E. Achenbach, *J. Power Sources*, **49** (1994) 333–348.
[29] J. R. Ferguson, J. M. Fiard and R. Herbin, *J. Power Sources*, **58** (1996) 109–122.
[30] J. Yuan, M. Rokni and B. Sunden, in *Solid Oxide Fuel Cells VI*, eds. S. C. Singhal and M. Dokiya, The Electrochemical Society Proceedings, Pennington, NJ, PV99-19, 1999, pp. 1099–1108.
[31] H. Yakabe, M. Hishinuma, M. Uratani, Y. Matsuzaki and I. Yasuda, *J. Power Sources*, **86** (2000) 423–431.
[32] M. Iwata, T. Hikosaka, M. Morita, T. Iwanari, K. Ito, K. Onda, Y. Esaki, Y. Sakaki and S. Nagata, *Solid State Ionics*, **132** (2000) 297–308.
[33] S. Kjelstrup Ratkje and K. S. Forland, *J. Electrochem. Soc.*, **138** (1991) 2374–2376.
[34] C. Haynes and W. J. Wepfer, *Energy Conversion & Management*, **41** (2000) 1123–1139.
[35] K. W. Bedringas, I. S. Ertesvag, S. Byggstoyl and B. F. Magnussen, *Energy*, **22** (1997) 403–412.
[36] J. Pålsson, A. Selimovic and L. Sjunnesson, *J. Power Sources*, **86** (2000) 442–448.
[37] W. G. Winkler, in *Solid Oxide Fuel Cells VI*, eds. S. C. Singhal and M. Dokiya, The Electrochemical Society Proceedings, Pennington, NJ, PV99-19, 1999, pp. 1150–1159.
[38] W. Winkler and H. Lorenz, in *Solid Oxide Fuel Cells VII*, eds. H. Yokokawa and S. C. Singhal, The Electrochemical Society Proceedings, Pennington, NJ, PV-2001-16, 2001, pp.196–204.
[39] A. Atkinson and A. Selcuk, *Acta Mater.*, **47** (1999) 867–874.

[40] J. W. Hutchinson and A. G. Evans, *Surface and Coatings Technology*, **149** (2002) 179–184.
[41] S. P. Simner and J. W. Stevenson, *J. Power Sources*, **102** (2001) 310–316.
[42] S. Taniguchi, M. Kadowaki, T. Yasuo, Y. Akiyama, Y. Miyake and K. Nishio, *J. Power Sources*, **90** (2000) 163–169.
[43] I. Yasuda and M. Hishinuma, in *Solid Oxide Fuel Cells IV*, eds. M. Dokiya, O. Yamamoto, H. Tagawa and S. C. Singhal, The Electrochemical Society Proceedings, Pennington, NJ, PV95-1, 1995, 924–933.
[44] K. Z. Fung and A. V. Virkar, in *Solid Oxide Fuel Cells IV*, eds. M. Dokiya, O. Yamamoto, H. Tagawa and S. C. Singhal, The Electrochemical Society Proceedings, Pennington, NJ, PV95-1, 1995, pp.1105–1114.
[45] C. W. Tanner, K. Z. Fung and A. V. Virkar, *J. Electrochem. Soc.*, **144** (1997) 21–30.
[46] F. Zhao, Y. Jiang, G. Y. Lin and A. V. Virkar, in *Solid Oxide Fuel Cells VII*, eds. H. Yokokawa and S. C. Singhal, The Electrochemical Society Proceedings, Pennington, NJ, PV2001-16, 2001, pp. 501–510.
[47] J. W. Kim, A. V. Virkar, K. Z. Fung, K. Mehta and S. C. Singhal, *J. Electrochem. Soc.*, **146** (1999) 69–78.
[48] T. Ackmann, L. G. J. de Haart, W. Lehnert and F. Thom, in *Proceedings of the 4th European SOFC Forum*, ed. A. J. McEvoy, Switzerland, 2000, pp. 431–438.
[49] J. Yuan, M. Rokni and B. Sunden, in *Proceedings of the Fifth European SOFC Forum*, ed. J. Huijsmans, Switzerland, 2002, pp. 921–928.
[50] J. Newman and C. W. Tobias, *J. Electrochem. Soc.*, **109** (1962) 1183–1191.
[51] Y. C. Hsiao, Porous anode with internal reforming in a SOFC: Modeling analysis, MS thesis, IIT, Chicago (1992).
[52] S. Al-Hallaj and J. R. Selman, Porous-electrode model for SOFC electrodes, in *Proceedings NETL Workshop on Fuel Cell Modeling*, U.S. Department of Energy, National Energy Technology Laboratory, Morgantown, PA., 2000.
[53] M. L. Perry, J. Newman and E. J. Cairns, *J. Electrochem. Soc.*, **145** (1998) 5–15.
[54] P. Costamagna, P. Costa and V. Antonucci, *Electrochim. Acta*, **43** (1998) 375–394.
[55] S. H. Chao and Z. T. Xia, *J. Electrochem. Soc.*, **148** (2001) A388–A394.
[56] S. Sunde, *J. Electrochem. Soc.*, **143** (1996) 1123–1132.
[57] S. Sunde, *J. Electrochem. Soc.*, **143** (1996) 1930–1939.
[58] S. Sunde, *J. Electroceramics*, **5** (2000) 153–182.
[59] J. Abel, A. A. Kornyshev and W. Lehnerts, *J. Electrochem Soc.*, **144** (1997) 4253–4259.
[60] F. H. van Heuveln, Characterisation of porous cathodes for application in solid oxide fuel cells, Doctoral dissertation, University of Twente,

Netherlands, Appendix: The electrode configuration of a three-electrode cell (1995), pp. 167–183.

[61] J. Winkler, P. V. Hendriksen, N. Bonanos and M. Mogensen, *J. Electrochem. Soc.*, **145** (1998) 1184–1192.

[62] J. Fleig and J. Maier, in *Solid Oxide Fuel Cells V*, eds. U. Stimming, S. C. Singhal, H. Tagawa and W. Lehnert, The Electrochemical Society Proceedings, Pennington, NJ, PV97-40, 1997, pp. 1374–1383.

[63] S. Primdahl, P. Hendriksen, P. Larsen, B. Kindl and M. Mogensen, in *Solid Oxide Fuel Cells VII*, eds. H. Yokokawa and S. C. Singhal, The Electrochemical Society Proceedings, Pennington, NJ, PV2001-16, 2001 pp. 932–941.

[64] H. Schichlein, M. Feuerstein, A. Müller, A. Weber, A. Krügel and E. Ivers-Tiffée, in *Solid Oxide Fuel Cells VI*, eds. S. C. Singhal and M. Dokiya, The Electrochemical Society, Pennington, NJ, PV99-19, 1999, pp. 1069–1077.

[65] A. Weber, A. Müller, D. Herbstritt and E. Ivers-Tiffée, in *Solid Oxide Fuel Cells VII*, eds. H. Yokokawa and S. C. Singhal, The Electrochemical Society Proceedings, Pennington NJ, PV2001-16, 2001, pp. 952–962.

[66] A. Bieberle, The electrochemistry of solid oxide fuel cell anodes: experiments, modeling, and simulation, Doctoral dissertation, ETH Zürich, Ch. 2, The state-space modeling approach, 2000, pp. 28–37.

[67] A. Mitterdorfer and L. J. Gauckler, *Solid State Ionics*, **117** (1999) 187–202.

[68] A. Mitterdorfer and L. J. Gauckler, *Solid State Ionics*, **117** (1999) 203–218.

[69] M. Prestat and L. J. Gauckler, in *Solid Oxide Fuel Cells VII*, eds. H. Yokokawa and S. C. Singhal, The Electrochemical Society Proceedings, Pennington, NJ, PV2001-16, 2001, pp. 574–582.

[70] I. Reiss, in, *CRC Handbook of Solid State Electrochemistry*, eds. P. J. Gellings and H. J. M. Bouwmeester, Ch. VII, 1997, pp. 223–268.

[71] S. Yuan and U. Pal, *J. Electrochem. Soc.*, **143** (1996) 3214–3222.

[72] P. Soral, U. Pal and W. Worrell, *J. Electrochem. Soc.*, **145** (1998) 99–106.

[73] S. Diethelm, A. Closset, J. van Herle and K. Nisancogliu, *Electrochemistry Japan (Denki Kagaku)*, **68** (2000) 444.

[74] S. Sunde, K. Nisancogliu and T. Gür, *J. Electrochem. Soc.*, **143** (1996) 3497–3504.

[75] S. Diethelm, Electrochemical characterization of oxygen transport and nonstoichiometry in mixed conducting perovskite-type oxides, Doctoral dissertation, EPFL Lausanne (2001), Ch. 5, 6.

[76] C. Fisher, H. Matsubara, *Computational Mater. Sci.*, **14** (1999) 177–184.

[77] G. E. Murch, C. R. Catlow and A. D. Murray, *Solid State Ionics*, **18/19** (1986) 196.

[78] Z. Lin, J. Jaffe and A. Hess, *J. Phys. Chem. A*, **103** (1999) 2117–2127.

[79] J. Snyder, J. Jaffe, Z. Lin, A. Hess and M. Gutowski, *Surf. Sci.*, **445** (2000) 495–505.
[80] T. Kato, S. Y. Kang, X. Xu and T. Yamabe, *J. Phys. Chem. B*, **105** (2001) 10340–10347.
[81] R. Car and M. Parrinello, *Phys. Rev. Lett.*, **55** (1985) 2471–2474.
[82] Z. Lin and J. Harris, *J. Phys. Condens. Matter*, **5** (1993) 1055–1080.
[83] W. M. C. Foulkes, *Phys. Rev. B*, **48** (1993) 14216–14225.